INFORMATION TO USERS

This manuscript has been reproduced from the microfilm master. UMI films the text directly from the original or copy submitted. Thus, some thesis and dissertation copies are in typewriter face, while others may be from any type of computer printer.

The quality of this reproduction is dependent upon the quality of the copy submitted. Broken or indistinct print, colored or poor quality illustrations and photographs, print bleedthrough, substandard margins, and improper alignment can adversely affect reproduction.

In the unlikely event that the author did not send UMI a complete manuscript and there are missing pages, these will be noted. Also, if unauthorized copyright material had to be removed, a note will indicate the deletion.

Oversize materials (e.g., maps, drawings, charts) are reproduced by sectioning the original, beginning at the upper left-hand corner and continuing from left to right in equal sections with small overlaps.

ProQuest Information and Learning
300 North Zeeb Road, Ann Arbor, MI 48106-1346 USA
800-521-0600

ELECTRON NUCLEAR DOUBLE RESONANCE OF $^{57}Fe^{3+}$ IN RUBIDIUM ALUMS

by

Jean-Robert Brisson

Thesis submitted to the School of Graduate Studies of the University of Ottawa in partial fulfillment of the requirements for the degree of Master of Science

Department of Physics
Faculty of Science and Engineering
University of Ottawa
Ottawa, Canada

1977

Acknowledgment

I would like to express my appreciation to Dr. Armen Manoogian who contributed greatly to my thesis during its development. I would also like to acknowledge the cheerful and skillful help of Bei Wah Chan, our technician, in the operation of the spectrometer.

INDEX

List of Figures

List of Tables

ABSTRACT

The electron-nuclear double resonance (ENDOR) spectrum of $^{57}Fe^{3+}$ in the two alums $RbAl(SO_4)_2 \cdot 12H_2O$ and $RbGa(SO_4)_2 \cdot 12H_2O$ is examined at ~9.4 GHz and 4.2 K. With the magnetic field in a general direction of the crystals, the ENDOR spectra of the four sites in the unit cell of the crystals were observed. A spin Hamiltonian expressed in trigonal form adequately described the observed frequencies of the four sites for the magnetic field in two directions. The hyperfine parameters were found to be slightly anisotropic. The nuclear spectroscopic splitting factor g_I was found to be isotropic within experimental error, with a value of $g_I = 0.180 \pm 0.004$. An additional term of the type S^3I was required for a successful fit of the experimental results to the spin Hamiltonian. The parameters are compared with those obtained by others in EPR or ENDOR studies of $^{57}Fe^{3+}$ in different crystals systems.

CHAPTER 1

INTRODUCTION

During the past few years there has been an interest in this laboratory to employ the principles of electron-nuclear double resonance (ENDOR) to study the paramagnetic impurity $^{53}Cr^{3+}$ ion in hydrated crystals of alums, guanidine salts and $AlCl_3 \cdot 6H_2O$. These crystals have a common property in that they all contain trivalent metallic ions surrounded by a trigonally distorted octahedron of water molecules, forming the complex $M^{3+} \cdot 6H_2O$. In the present work an ENDOR study is made of the $^{57}Fe^{3+}$ ion doped as a small impurity in the two alums $RbAl(SO_4)_2 \cdot 12H_2O$ and $RbGa(SO_4)_2 \cdot 12H_2O$. The study is done at a temperature of 4.2 K and a microwave frequency of~9.4 GHz (X-band). To perform ENDOR the atom must possess a nuclear spin, and the value for ^{57}Fe is $I = \frac{1}{2}$. The isotopic abundance of the ^{57}Fe isotope is normally ~2%, but in this work the isotope enriched to 96% was used.

The rubidium alums are chosen as the host lattice because they produce a relatively small splitting of the Fe^{3+} electron paramagnetic resonance (EPR) lines. Hence a symmetric pattern of EPR spectral lines is obtained for all magnetic field directions at the crystal, simplifying the study and interpretation of the results. In contrast for the cesium alums, guanidine salts and $AlCl_3 \cdot 6H_2O$, large zero field splittings at the Fe^{3+} ion sites cause the EPR transitions to fall in the crossing point region of the energy levels, giving rise to a complicated and asymmetric EPR pattern spread over a large magnetic field range.

The ground state electron configuration of the free Fe^{3+} ion is (argon core)$(3d^5)$ which, according to Hund's rules, gives rise to a $^6S_{5/2}$ sextet term with an electronic spin of $S = 5/2$. Hence Fe^{3+} is called an S-state ion. The interaction of the Fe^{3+} ion with the electrostatic field of the surrounding atoms in a crystal causes a splitting of the ground state sextet, leaving groups of smaller degeneracy. This degeneracy within each group depends on the symmetry of the electrostatic field at the paramagnetic ion site, and thus can be predicted by group theory. In alums, the

trigonal distortion of the six waters coordinated to the Fe^{3+} ion reduces the symmetry from cubic to three-fold symmetry about the trigonal axis. Fig. 1.1 shows the positions of the cubic field axes (xi, eta, zeta) and the trigonal axis z in the octahedron, as used in EPR studies.

A cubic crystalline electric field splits the $^6S_{5/2}$ sextet into a quadruplet and a doublet. The separation between the two groups is usually denoted as 3a, with a being called the cubic field splitting parameter. The degeneracy remaining in the groups can be lifted by a magnetic field, whose action on the electronic spin levels is described by the electronic spectroscopic splitting parameter g [1]. The resulting spin levels labeled by the magnetic quantum number M are shown in Fig. 1.2.

Trigonal symmetry causes the sextet to be split into three doublets with energy levels given by the following expressions[2] :

$$W_{1,2} = -\frac{1}{2}(a-F) + \frac{1}{3}D \pm \frac{1}{6}[\,(18D + a - F)^2 + 80a^2\,]^{\frac{1}{2}}$$

$$W_3 = (a-F) - \frac{2}{3}D \quad ,$$

where D and F are axial splitting parameters for second and fourth order energy terms. These levels, known as the fine structure, are split at most by a few cm^{-1} in energy. The energy level diagram showing the splitting for various symmetries is given in Fig. 1.3. The next highest excited state of Fe^{3+} is about 10^3 cm^{-1} above the ground state.

Electron paramagnetic resonance occurs when microwave radiation of frequency υ and energy $h\upsilon$ induces transitions from the M to the M+1 level within the ground manifold (Fig. 1.2). Or, stated alternatively, allowed transitions occur when the selection rule $\Delta M=\pm 1$ is obeyed. With υ fixed, the magnetic fields at which the transitions occur are found by detecting the energy absorption at resonance using a microwave bridge. The intensity of a transition is determined primarily by the difference in population between the more heavily populated lower level and the upper level involved.

Since $^{57}Fe^{3+}$ has a nuclear spin of $I = \frac{1}{2}$, the interaction of the nuclear and electronic spins will produce hyperfine splittings. The nuclear

levels arising from this interaction are labeled by the quantum number m, and are shown in Fig. 1.2. The hyperfine splittings can be detected by the ENDOR technique. In this method a strong microwave power is applied to an EPR line so as to partially saturate it. Transitions between the $m = \frac{1}{2}$ and $m = -\frac{1}{2}$ nuclear levels are then induced by sweeping with a strong radio frequency field. This produces a noticeable change in the population of the electronic levels. Thus the nuclear transition is detected by the consequent change in intensity of the much stronger EPR signal.

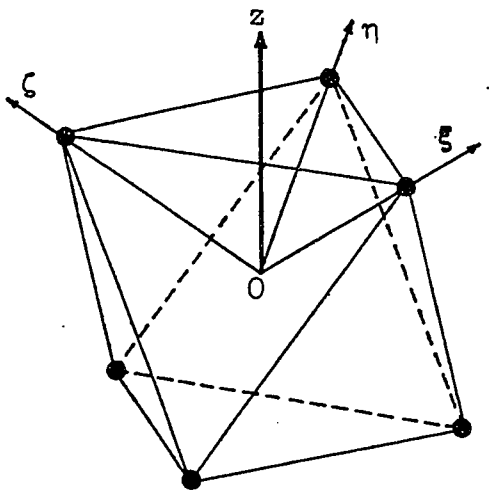

Fig. 1.1 Regular octahedron showing the cubic field axes $\xi\eta\zeta$ and the trigonal axis z. The trivalent ion is at the center of the octahedron, marked O.

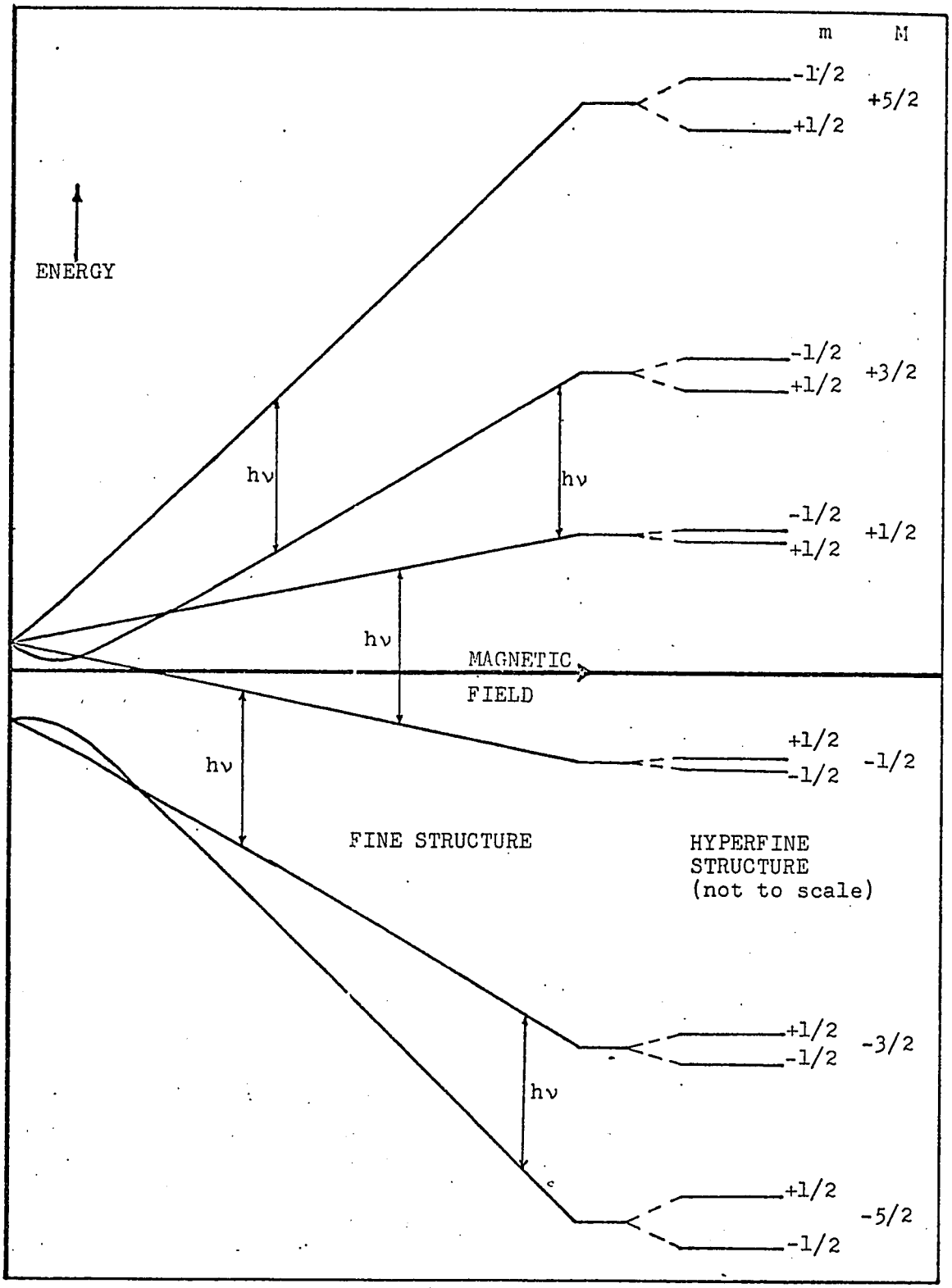

Fig. 1.2 Energy levels for cubic symmetry and S = 5/2. $\vec{H}$ is along a cubic field axis, with $\underline{a} > 0$.

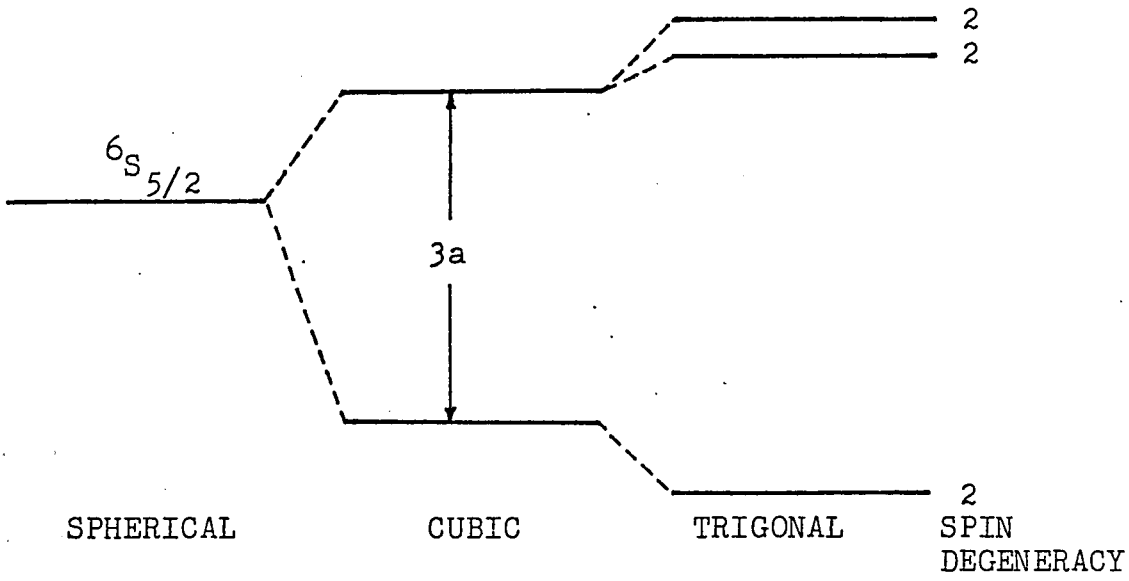

Fig. 1.3 Ground state splitting for various symmetries, with a > 0 and D < 0.

CHAPTER 2

EXPERIMENTAL TECHNIQUE

In the following sections an outline is given on the detection of the resonance signal. An excellent reference to the subject is the book by Poole [3].

2.1 EPR Signal Detection

A block diagram of the spectrometer, built by Danilov and Manoogian [4], is shown in Fig. 2.1. The source of microwave energy is a reflex klystron. The sample is in a resonant cavity which amplifies the microwave field at the sample. The klystron frequency is tuned to the cavity frequency by minimizing the crystal detector signal in the cavity arm of the microwave bridge. The klystron frequency is stabilized electronically by a microwave oscillator stabilizer (MOS). At resonance, microwave power is absorbed by the sample and the power level in the

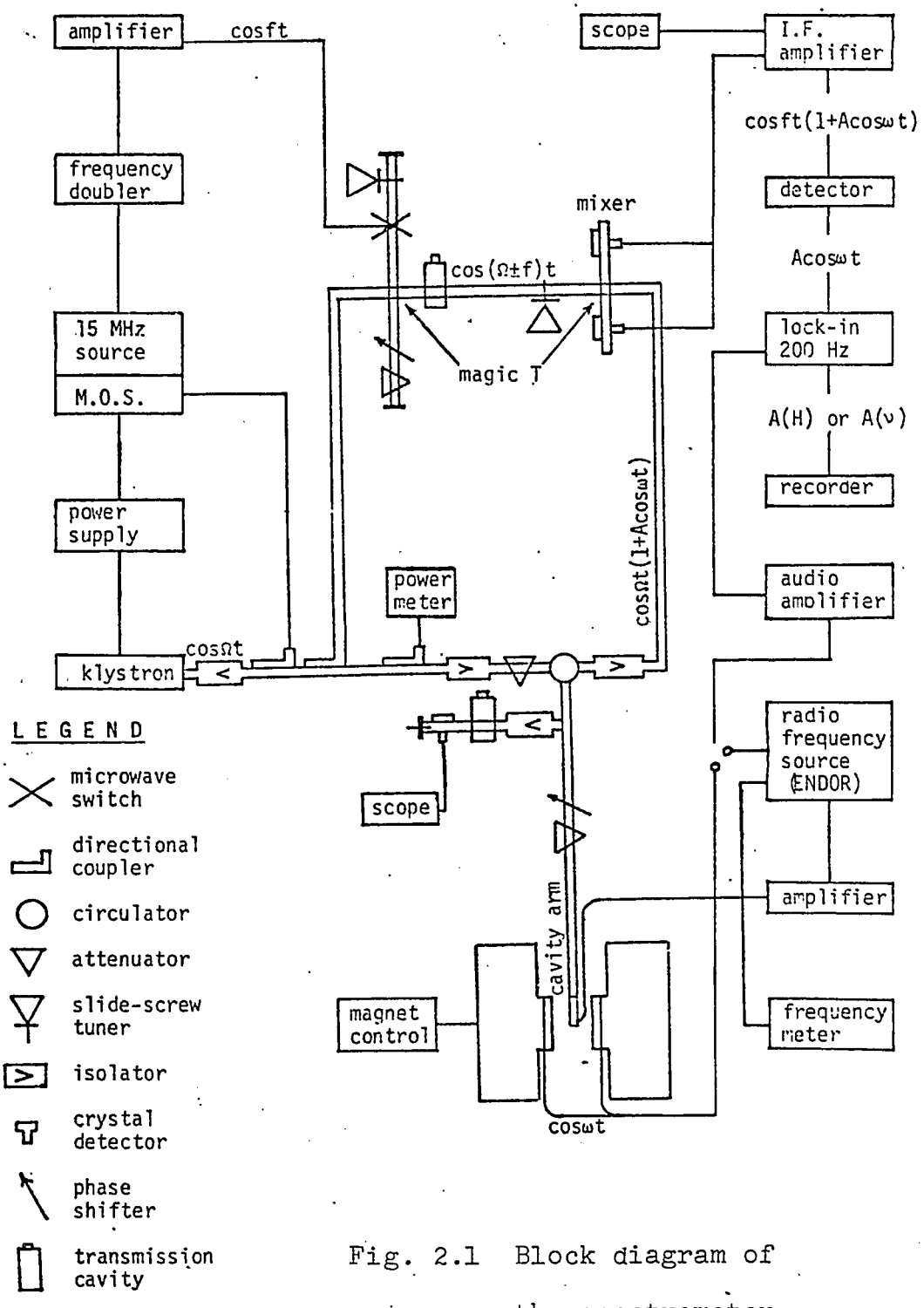

Fig. 2.1 Block diagram of the spectrometer

cavity changes. The absorption mode is selected by a proper adjustment of the attenuator and phase shifter in the cavity arm.

The steady external magnetic field H is modulated at a frequency of ω = 200 Hz by means of a signal obtained from the lock-in amplifier, which is applied to Helmholtz coils mounted on the magnet pole pieces. The value of the total external magnetic field H' is then given by the expression

$$H' = H + h\cos\omega t,$$

where h is the modulation amplitude with a value of about 5×10^{-4} tesla. If v(H) is the normalized absorption curve (Fig. 2.2), then the resonance signal can be written as a modulation on the carrier by [5]

$$v(H')\cos\Omega t,$$

where Ω is the microwave frequency. Using a Taylor's series expansion, v(H') can be written as

$$1 + \frac{h^2}{4} v''(H) + [\, v'(H) + \frac{h^2}{8} v'''(H) \,]h\cos\omega t + \ldots$$

where $v'(H) = \left(\frac{dv}{dH}\right)_H$, and etc.

Since h is small compared to the linewidth ($\sim 20 \times 10^{-4}$

tesla) then

$$v(H') \rightarrow 1 + v'(H)h\cos\omega t \rightarrow 1 + A\cos\omega t \ .$$

The signal

$$(1 + A\cos\omega t)\cos\Omega t$$

at resonance enters the "magic T" of the balanced mixer where it is mixed with a sideband ($\Omega \pm f$) which is 30 MHz removed from the klystron's carrier frequency. The sideband is produced by amplitude modulation of the carrier with the aid of a microwave switch placed in the waveguide line. The intermediate frequency of 30 MHz amplitude modulated at 200 Hz, given by the expression

$$\cos ft(1 + A\cos\omega t) \ ,$$

is detected by the balanced mixer. The use of the high intermediate frequency at 30 MHz reduces the noise of detection, since this effect is inversely proportional to the detection frequency. The signal is then amplified by passing through a high gain 30 MHz amplifier strip. The last stage of the amplifier demodulates the signal to produce the 200 Hz component, which is sent to the lock-in amplifier. The lock-in amplifier produces the first derivative of the absorption

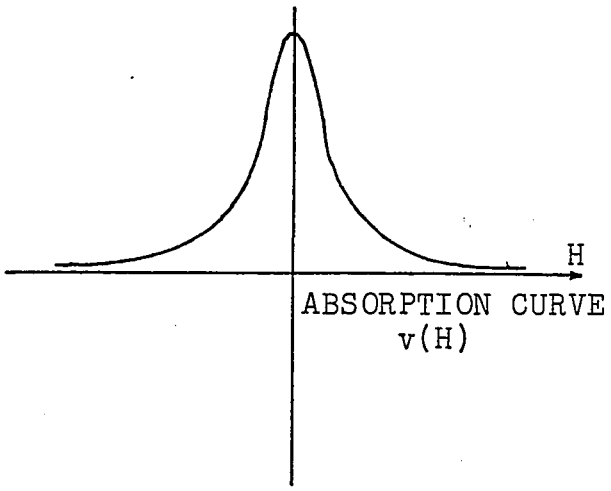

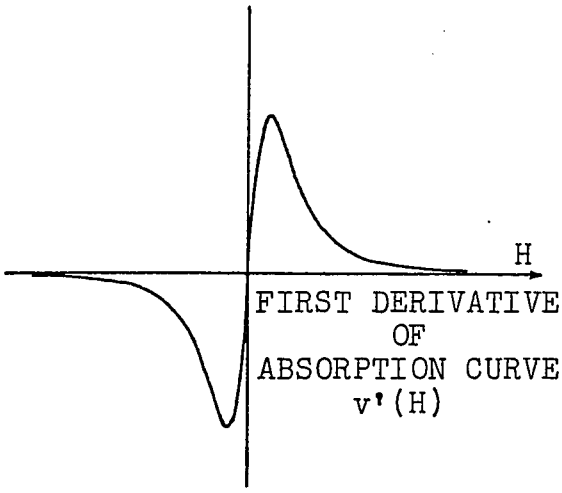

Fig. 2.2 Absorption curve and its first derivative .

signal, as shown in Fig. 2.2, which is traced on a chart recorder.

The strength of the external magnetic field H was measured using a proton nuclear magnetic resonance (NMR) gaussmeter. The measurements were taken at the center of the EPR lines. The NMR system detects the hydrogen nuclear resonance of water used as a probe. The frequency at which the proton resonance occurs is measured with a frequency counter. The magnetic field value of the resonance is then calculated from the relation

$$H(\text{tesla}) = \frac{\nu(\text{MHz})}{42.5759} ,$$

where ν is the proton resonance frequency and 42.5759 is the frequency for proton resonance in a 1 tesla magnetic field.

2.2 ENDOR Signal Detection

To obtain an ENDOR signal the steady magnetic field is set on an EPR line and the power level in the microwave cavity is increased so as to partially saturate the line. The 200 Hz modulation to the Helmholtz coils on the magnetic pole pieces is then switched

off. A radio frequency (rf) field is applied to the sample via a two turn coil of wire placed around it inside the cavity. The 200 Hz modulation signal from the lock-in amplifier is applied to the rf power with a deviation of 75 kHz. Nuclear transitions are promoted by sweeping the the rf oscillator through the desired frequency range. The detection of the ENDOR signal at resonance is then the same as described above for the EPR transitions. The derivative of the absorption curve with respect to frequency is produced on the strip chart recorder. The rf frequencies at which ENDOR transitions occur are read off a frequency counter. The rf modulation is switched off when making the measurements.

2.3 Microwave Cavity System

The microwave cavity used in both the EPR and ENDOR work is shown in Fig. 2.3. The cavity operated in the TE_{014} mode. The two turn copper coil for promoting ENDOR transitions is wrapped around a carefully machined holder made of Delrin. This material is a mixture of Teflon and Nylon. It is easy to machine, is non-lossy, and maintains its shape and dimensions upon cycling

between 4.2 K and room temperature. The leads of the copper coil pass through a small hole in the cavity wall and are connected to a coaxial cable. For liquid helium operation the cavity is placed in a double dewar system, with liquid helium in the inner dewar and liquid nitrogen in the outer one. The liquid helium filled the cavity and associated waveguide arm . This arrangement permitted about six hours of operation without refilling the liquid helium.

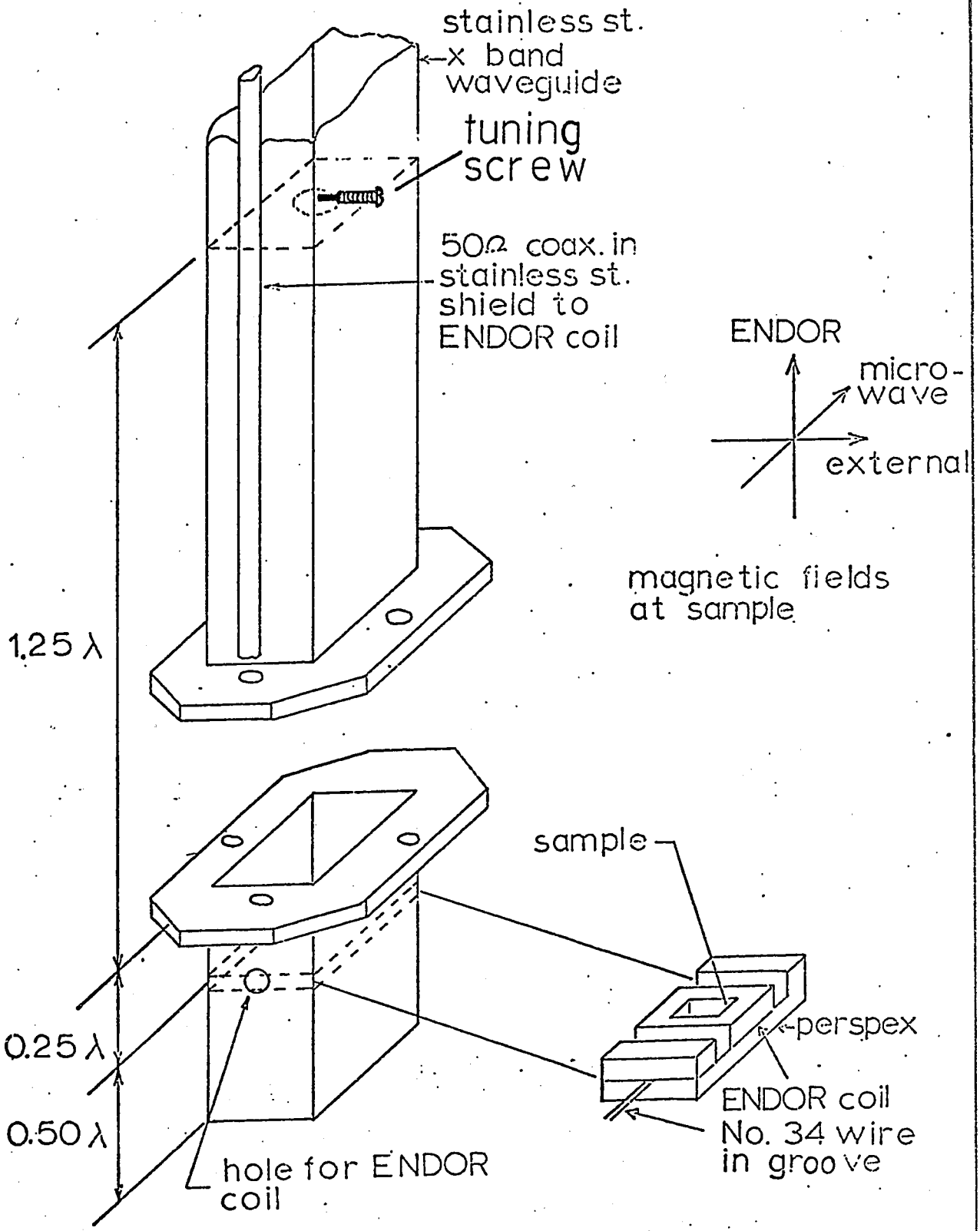

Fig. 2.3 ENDOR X-band cavity, showing the sample holder and the coil support, and the magnetic fields at the sample.

CHAPTER 3

EPR THEORY AND RESULTS

3.1 Crystallography

The alum structure has been described in detail by Lipson [6], Lipson and Beevers [7], and by Bacon and Gardner [8]. The structure is cubic with point group $\frac{2}{m}3$ and space group Pa3. There are four trivalent ions per unit cell at positions

$$(0\ 0\ 0),\ (0\ \tfrac{1}{2}\ \tfrac{1}{2}),\ (\tfrac{1}{2}\ 0\ \tfrac{1}{2}),\ (\tfrac{1}{2}\ \tfrac{1}{2}\ 0),$$

each being surrounded by an octahedron of water molecules. The positions of the water molecules are given by the set $\langle v\ \bar{v}\ u\rangle$, where $v \sim 0.02$ and $u \sim 0.16$. Each octahedron is distorted along a trigonal axis which coincides with one of the $\langle 111\rangle$ axes of the crystal. Thus the $\xi\eta\zeta$ axes (Fig. 1.1) of the cubic field do not coincide with the positions of the water molecules.

Each octahedron is rotated about the trigonal axis by an angle α. Hence each trivalent ion site will have a different set of $\xi\eta\zeta$ axes which do not coincide

with the cubic crystallographic ⟨100⟩ axes. The direction cosines (e,f,d) of the ζ axes with respect to the ⟨100⟩ axes for each site are given in the table of Fig. 3.1. For small rotations about the trigonal axis, the position of the ξηζ axes will be near the {110} planes as shown in the stereogram of Fig. 3.1. The relationship between these axes, the angle of rotation α, and the positions of the water molecules, are derived in appendix 1.

The crystals were grown from a stochiometric solution of the constituent salts, and they had well developed faces, mostly corresponding to {111} and {100} planes. These faces were identified by measuring the angles between the planes with a goniometer. Hence the {110}planes are easily found, since they contain the ⟨001⟩ and the ⟨111⟩ directions.

3.2 Spin Hamiltonian Describing the EPR Spectrum

To describe the energy levels of the ground state manifold, an effective Hamiltonian, called the spin Hamiltonian, was introduced by Pryce [9]. The Hamiltonian operates only on the effective spin functions

SITE	POSITION OF SITE	TRIGONAL AXIS	ANGLE OF ROTATION ABOUT THE TRIGONAL AXIS	ζ AXIS
A	(0 0 0)	111	$\|\alpha\|$	efd
B	(½ ½ 0)	$\bar{1}11$	$-\|\alpha\|$	$\bar{e}fd$
C	(½ 0 ½)	$\bar{1}\bar{1}1$	$\|\alpha\|$	$\bar{e}\bar{f}d$
D	(0 ½ ½)	$1\bar{1}1$	$-\|\alpha\|$	$e\bar{f}d$

$3d = 1+2\cos\alpha$

$3e = 1- \cos\alpha + \sqrt{3}\,|\sin\alpha|$

$3f = 1- \cos\alpha - \sqrt{3}\,|\sin\alpha|$

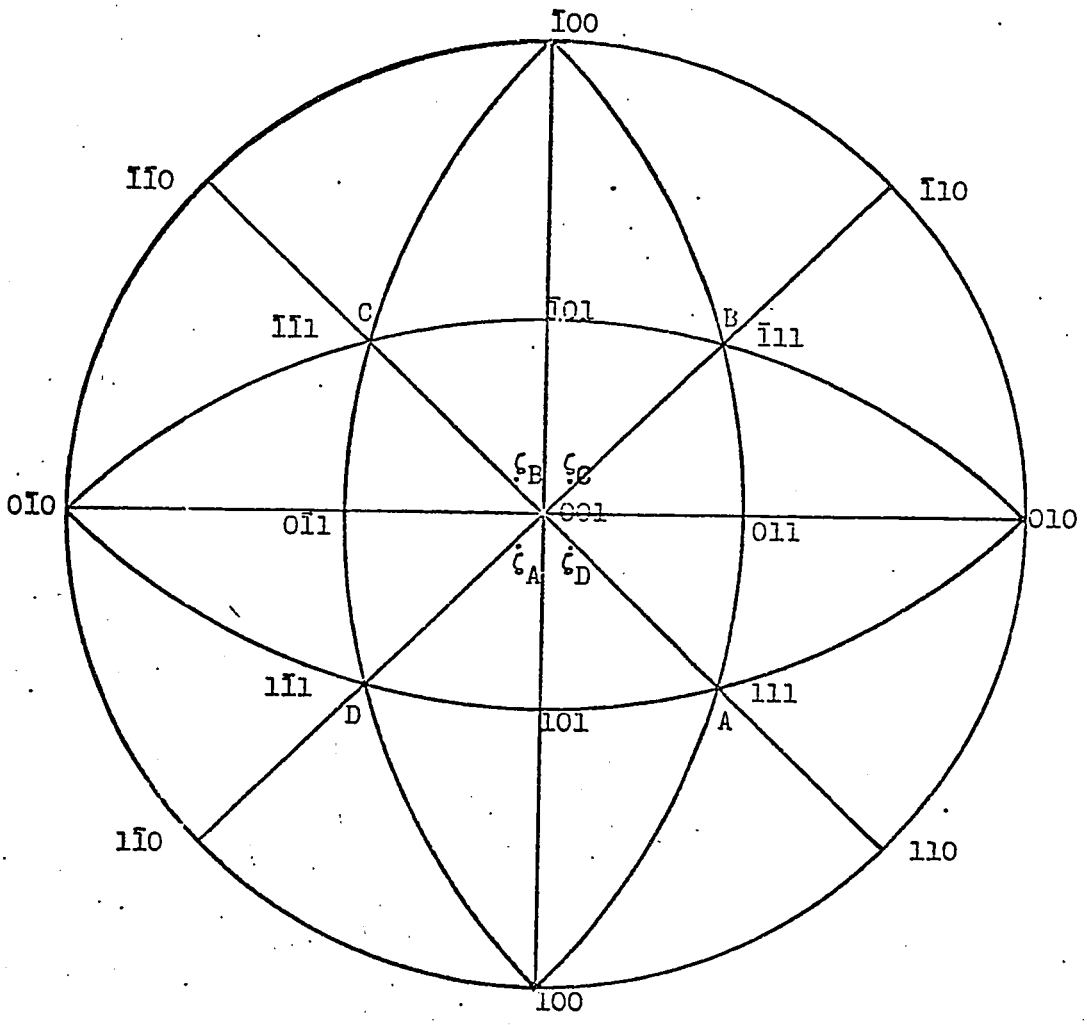

Fig. 3.1 Stereogram showing the position of the ζ axes in the rubidium alums(not to scale). The table at the top of the figure shows the direction cosines of the ζ axes with respect to the crystal ⟨100⟩ axes, for each site.

of the ground manifold. It consists of spin operators which make significant contribution to the paramagnetism. Each independent term in the spin Hamiltonian is multiplied by a parameter which in principle can be calculated theoretically. Each of these independent terms must be invariant under the point symmetry operations of the paramagnetic ion.

The spectrum of Fe^{3+} in alums was analyzed in terms of the following spin Hamiltonian given by Bleaney and Trenam [2] :

$$\mathcal{H} = g\beta\vec{H}\cdot\vec{S} + D\left[S_z^2 - \tfrac{1}{3}S(S+1) \right]$$

$$+ \frac{a}{6}\left[S_\xi^4+S_\eta^4+S_\zeta^4 - \tfrac{1}{5}S(S+1)(3S^2+3S-1) \right]$$

$$+ \frac{F}{180}\left[35S_z^4 -30S(S+1)S_z^2 +25S_z^2 -6S(S+1) +3S^2(S+1)^2 \right]$$

Here D and F correspond to axial fields of the second and fourth degree, respectively. The z axis is along one of the $\langle 111 \rangle$ directions of the crystal. The quantity a is the cubic field splitting parameter, and ξ, η, ζ are the axes of the cubic field, which are displaced from the crystallographic $\langle 100 \rangle$ axes by a rotation about the z axis.

The spin Hamiltonian is rewritten, as done by Geschwind [10], relative to a set of axes which more specifically expresses the point symmetry of the octahedral sites :

$$\mathcal{H} = g\beta H\cos\theta S_z + \frac{1}{2}g\beta H\sin\theta(S_+ + S_-) + D[\, S_z^2 - \tfrac{1}{3}S(S+1)\,]$$
$$- \frac{a-F}{180}[\, 35S_z^4 - 30S(S+1)S_z^2 + 25S_z^2 - 6S(S+1) + 3S^2(S+1)^2\,]$$
$$+ \frac{a\sqrt{2}}{36}[\, S_z(S_+^3 e^{i3(\varphi-\alpha)} + S_-^3 e^{-i3(\varphi-\alpha)})$$
$$+ (S_+^3 e^{i3(\varphi-\alpha)} + S_-^3 e^{-i3(\varphi-\alpha)})S_z\,] \quad ,$$

where $S_+ = S_x + iS_y$ and $S_- = S_x - iS_y$.

In this expression the z axis is along a ⟨111⟩ direction. The x axis is chosen to coincide with the projection of $\vec{H}$ upon a plane perpendicular to the z axis. The angles are defined as follows :

θ is the angle between the $\vec{H}$ and z directions,

α is the angle of rotation of the octahedron about the z axis,

φ is the angle between the projection of $\vec{H}$ in the trigonal plane, and the projection of the [001] axis in the same plane (a ⟨112⟩ axis).

Table 3.1 gives the angles which $\vec{H}$ makes with the different sites for an arbitrary direction of $\vec{H}$. Fig. 3.2 shows the projection of the cubic field axes and the [111] axis in the trigonal plane for each site.

3.3 Energy Levels

The energy levels to second order in perturbation theory are given by Bleaney and Trenam [2] in terms of the direction cosines of $\vec{H}$ with the cubic field axes. Here instead, they will be given in terms of θ and φ. Hence the field positions H, for resonance at a fixed microwave frequency υ, are found to be given by

$$\pm\tfrac{5}{2} \leftrightarrow \pm\tfrac{3}{2}: \; g\beta H = h\upsilon \mp [2D(3\cos^2\theta - 1) + 2pa + \tfrac{1}{6}Fq] - 32\delta_1 + 4\delta_2 + \varepsilon_1;$$

$$\pm\tfrac{3}{2} \leftrightarrow \pm\tfrac{1}{2}: \; g\beta H = h\upsilon \mp [D(3\cos^2\theta - 1) - \tfrac{5}{2}pa - \tfrac{5}{24}Fq] + 4\delta_1 - 5\delta_2 + \varepsilon_2;$$

$$+\tfrac{1}{2} \leftrightarrow -\tfrac{1}{2}: \; g\beta H = h\upsilon + 16\delta_1 - 8\delta_2 + \varepsilon_3;$$

where p is calculated by the method described in

section 4.1 and is given by the expression

$$p = -q/12 + \frac{1}{3}5\sqrt{2}\sin^3\theta\cos\theta\cos 3(\varphi-\alpha) \ .$$

The additional terms are given by Bleaney and Trenam [2] as

$$q = 35\cos^4\theta - 30\cos^2\theta + 3 \ ,$$

$$\delta_1 = \frac{D^2}{h\upsilon}\cos^2\theta\sin^2\theta \ ,$$

$$\delta_2 = \frac{D^2}{h\upsilon}\sin^4\theta \ ,$$

$$\epsilon_1 = \frac{a^2}{h\upsilon}[\ 5\sigma(1-7\sigma)/3] \ ,$$

$$\epsilon_2 = -\frac{a^2}{h\upsilon}[5(3+178\sigma-625\sigma^2)/48] \ ,$$

$$\epsilon_3 = \frac{a^2}{h\upsilon}[10\sigma(7-25\sigma)/3] \ ,$$

where $\sigma = (1-p)/5$.

Hence, with the magnetic field in a general direction, these expressions describe 20 lines corresponding to $\Delta M=\pm 1$ transitions, five for each nonequivalent site.

Table 3.1 Angles in the spin Hamiltonian for an arbitrary direction of $\vec{H}$.

SITE	TRIGONAL AXIS	ANGLE OF $\vec{H}$ WITH THE TRIGONAL AXIS θ	$\langle 112 \rangle$ AXIS	ANGLE OF $\vec{H}$ WITH THE $\langle 112 \rangle$ AXIS φ
A	111	$\arccos\left(\frac{S+R+T}{\sqrt{3}}\right)$	$\bar{1}\bar{1}2$	$\frac{R-T}{\lvert R-T\rvert}\arccos\left(\frac{2S-R-T}{2\sqrt{(1-TR-RS-ST)}}\right)$
B	$\bar{1}11$	$\arccos\left(\frac{S-R+T}{\sqrt{3}}\right)$	$1\bar{1}2$	$\frac{R+T}{\lvert R+T\rvert}\arccos\left(\frac{2S+R-T}{2\sqrt{(1+TR+RS-ST)}}\right)$
C	$\bar{1}\bar{1}1$	$\arccos\left(\frac{S-R-T}{\sqrt{3}}\right)$	112	$\frac{-R+T}{\lvert -R+T\rvert}\arccos\left(\frac{2S+R+T}{2\sqrt{(1-TR+RS+ST)}}\right)$
D	$1\bar{1}1$	$\arccos\left(\frac{S+R-T}{\sqrt{3}}\right)$	$\bar{1}12$	$\frac{-R-T}{\lvert -R-T\rvert}\arccos\left(\frac{2S-R+T}{2\sqrt{(1+TR-RS+ST)}}\right)$

$\vec{H}=(R,T,S)$ WHERE R,T,S ARE THE DIRECTION COSINES OF $\vec{H}$ WITH THE $\langle 100 \rangle$ AXES.

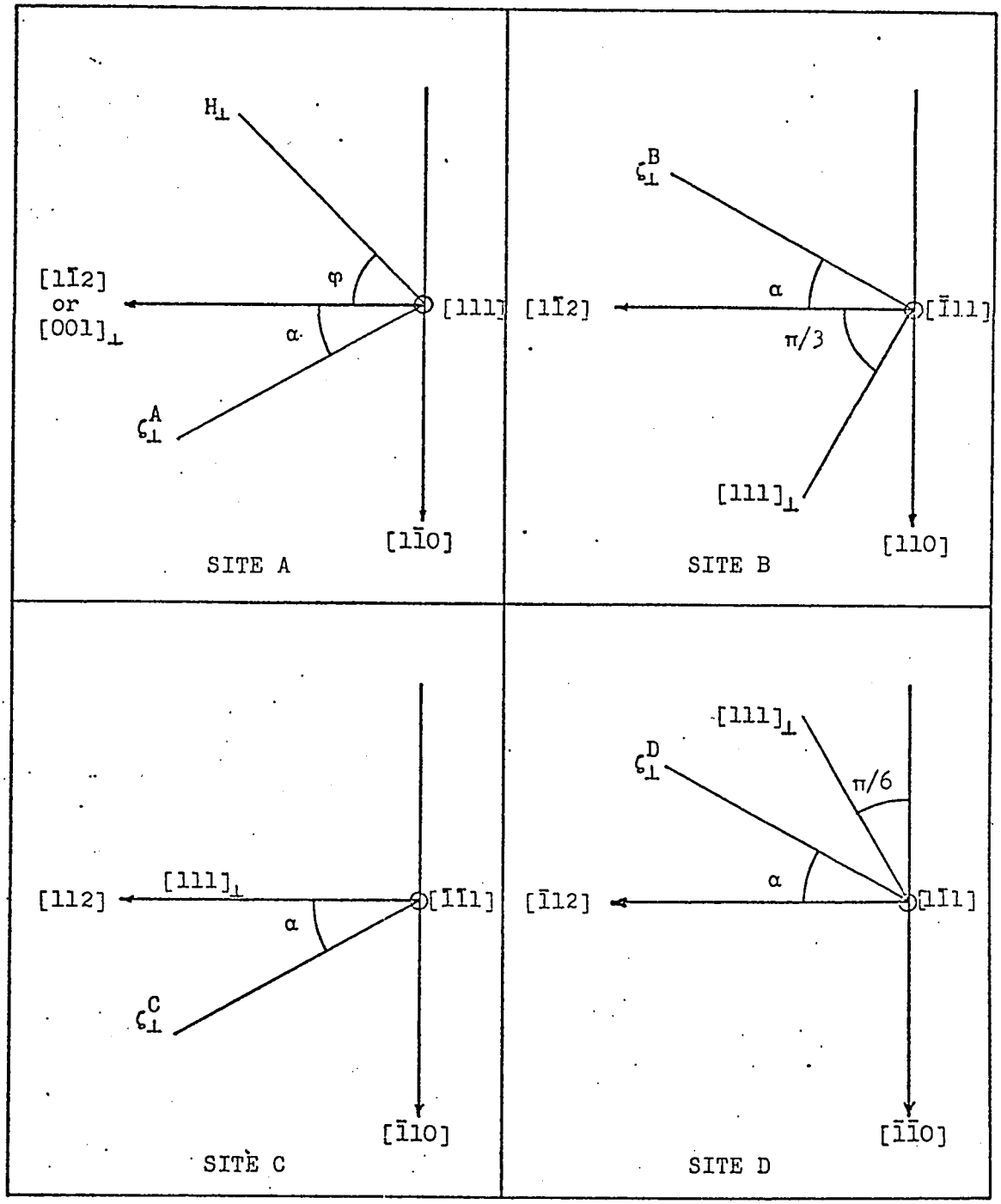

Fig. 3.2 Projection of the ζ axis, $\zeta_\perp$, and the projection of the [111] axis, $[111]_\perp$, in the trigonal planes of the four different sites. Angles are positive ccw and are all measured in the trigonal planes.

3.4 EPR Results

A. RbAl alum

The EPR spectrum of $RbAl(SO_4)_2 \cdot 12H_2O$ was studied in 1954 by Bleaney and Trenam [2]. However it must be restudied and understood before attempting ENDOR studies. The angular variation of the spectral lines in a {110} plane as observed by them was similar to the one shown in Fig. 3.3. Maxima in the field separation occur when the magnetic field is close to the cubic field axes and on a crystal ⟨111⟩ direction.

To evaluate the parameters in the spin Hamiltonian, measurements were taken along a trigonal axis, which is the [111] axis, and near a cubic field axis. For measurement near the ξηζ axes the magnetic field was rotated by a small angle in the (110) plane to maximize the field separation between the lines.

For $\vec{H}$ on a [111] axis, the trigonal axes of the remaining sites all make angles of 70.5° with the applied field, and their spectra coincide. For $\vec{H}$ near the cubic field axes 20 lines should be observed. Only about 10 of these were measured since all were not resolved due to line broadening. Typical spectra

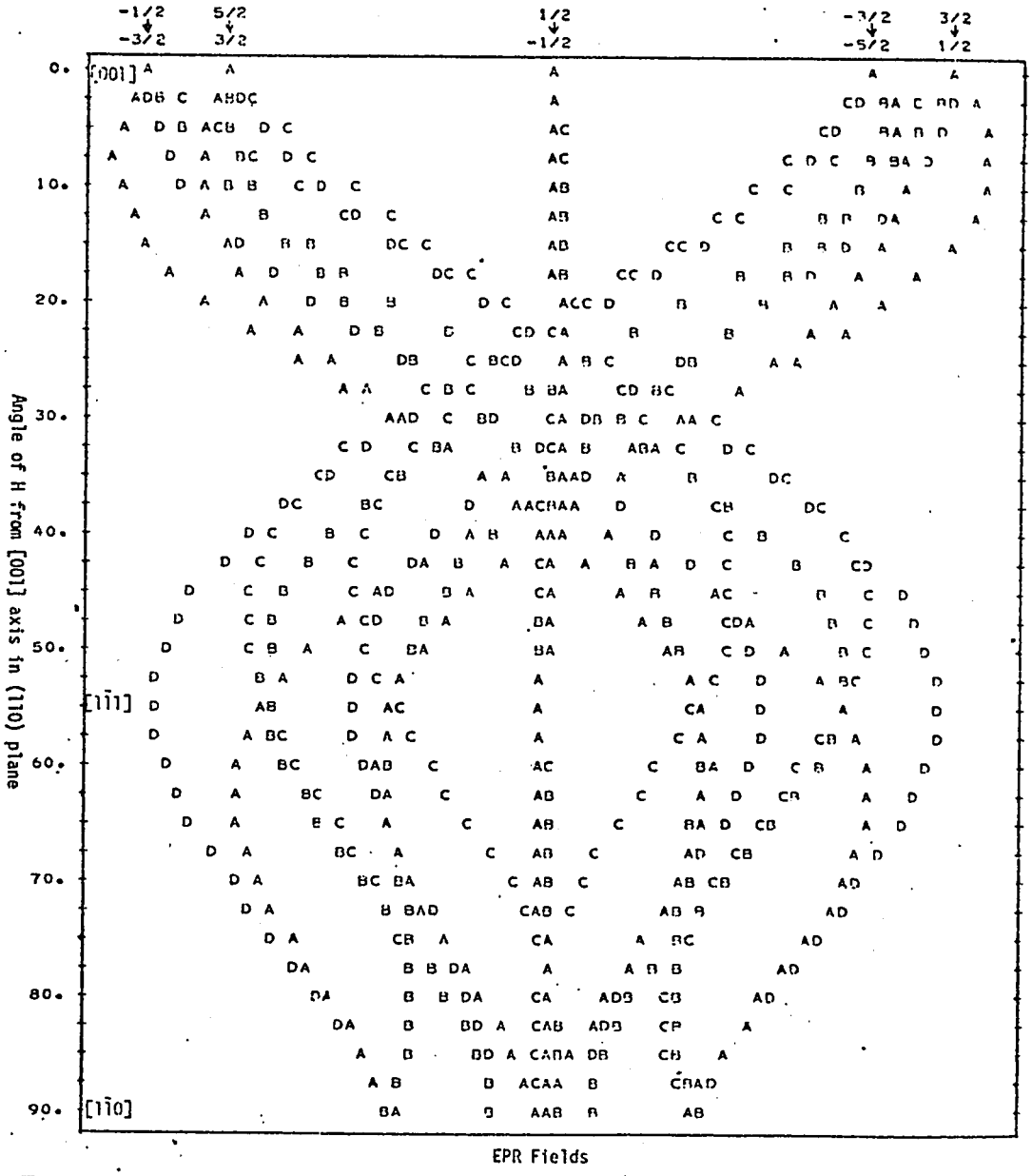

Fig. 3.3 Angular variation of the EPR spectrum for Fe^{3+} in RbAl alum, with $\vec{H}$ in the (110) plane.

are shown in Fig. 3.4. From the EPR transition equations of section 3.3, the splitting parameters were evaluated. Table 3.2 gives the values of these parameters and the EPR fields. At the bottom of the table is shown a sketch of the observed and calculated line positions which are listed in Table 3.2.

B. RbGa alum

For $RbGa(SO_4)_2 \cdot 12H_2O$ a more complete study of the EPR spectrum was made since this was not studied previously by other authors. Measurements were taken along a ⟨111⟩ direction, a ⟨110⟩ direction, and near a cubic field axis in the (110) plane. The spectra obtained are shown in Fig. 3.5.

From measurements near the cubic field axes, the cubic field splitting parameter $\underline{a}$ was found to be the same as in RbAl alum. In that direction the first order contribution of the D term, $(3\cos^2\theta-1)$, goes to zero. Hence, to first order, we have

$$H(\tfrac{3}{2}\leftrightarrow\tfrac{1}{2}) - H(-\tfrac{1}{2}\leftrightarrow-\tfrac{3}{2}) = 5(a - 7F/27) \cong 5a \ .$$

The magnetic field positions of the EPR lines as given by the equations in section 3.3 are plotted

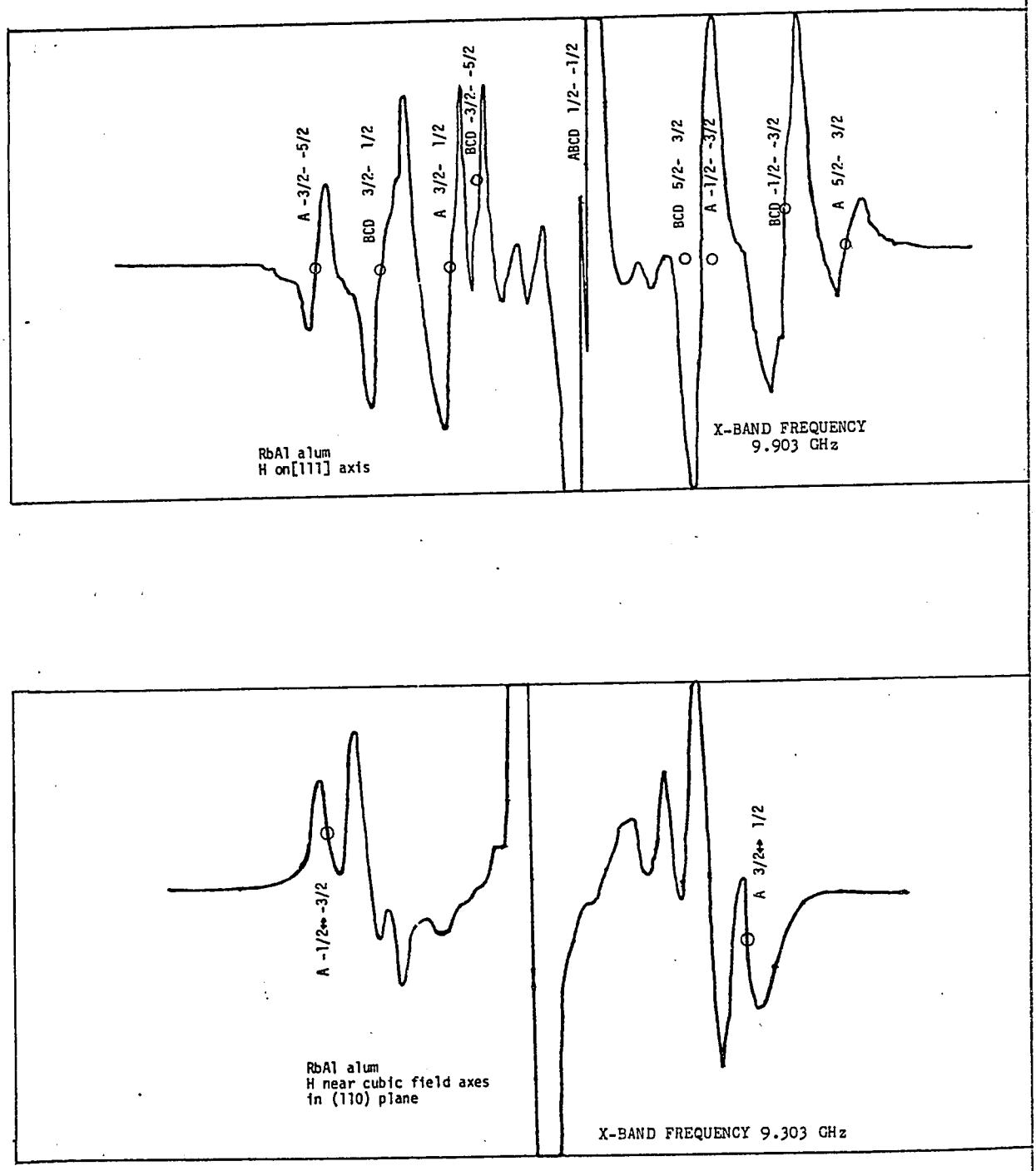

Fig. 3.4 EPR spectra for RbAl alum.

Table 3.2

PARAMETERS AND EPR FIELDS FOR Fe^{3+} IN $RbAl(SO_4)_2 \cdot 12\ H_2O$ AT 4.2 K

$g = 2.003$ $\quad |\alpha| = 9.5$ degrees

$a/g\beta = 0.142 \times 10^{-1}$ T $\quad D/g\beta = -0.033 \times 10^{-1}$ T $\quad F/g\beta = 0.004 \times 10^{-1}$ T

$a/hc = 133 \times 10^{-4}$ cm^{-1} $\quad D/hc = -31 \times 10^{-4}$ cm^{-1} $\quad F/hc = 4 \times 10^{-4}$ cm^{-1}

DIRECTION OF MAGNETIC FIELD	EPR FIELDS, H, 10^{-1} T										
	OBSERVED					CALCULATED					
H						SITE	$-\frac{1}{2} \to -\frac{3}{2}$	$+\frac{5}{2} \to +\frac{3}{2}$	$+\frac{1}{2} \to -\frac{1}{2}$	$-\frac{3}{2} \to -\frac{5}{2}$	$+\frac{3}{2} \to +\frac{1}{2}$
near ξηζ axes	2.97	3.02	3.33	3.61	3.66	A	2.97	3.03	3.32	3.60	3.66
polar coordinates						B	3.06	3.07	3.32	3.56	3.56
of H with ⟨100⟩ axes	3.14	3.08	3.33	3.55	3.50	C	3.12	3.16	3.33	3.47	3.50
(1,10.5,-47)						D	3.03	3.14	3.33	3.50	3.60
[111] axis	3.48	3.63	3.31	3.00	3.16	A	3.49	3.63	3.31	3.00	3.16
	3.56	3.47	3.32	3.19	3.08	BCD	3.55	3.44	3.31	3.19	3.09

PLOT OF EPR FIELDS FOR H NEAR ξηζ AXES

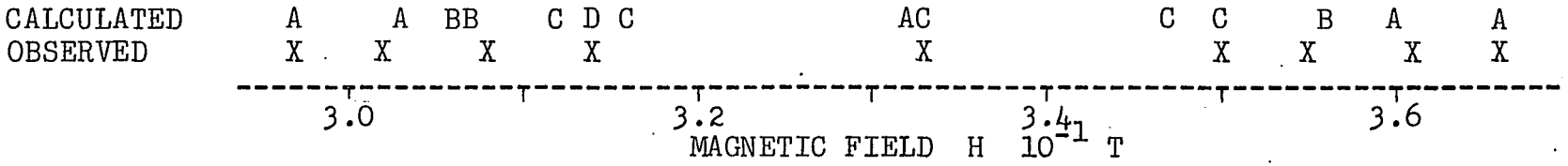

as a function of the D parameter for the [111] and [1$\bar{1}$0] directions, and are shown in Figs. 3.6 and 3.7, respectively. These diagrams were used in conjunction with the observed spectra to determine the value of D. The final values of the parameters were obtained by varying each parameter independently. The ones that gave the best agreement with the observed fields in the three directions measured are given in Table 3.3 along with the EPR fields. At the bottom of the table a sketch of the lines positions for $\vec{H}$ near a cubic field is given. The observed variation of the spectrum in a {110} plane compared to the calculated one using the parameters of table 3.3 are found to be qualitatively the same (Fig. 3.8).

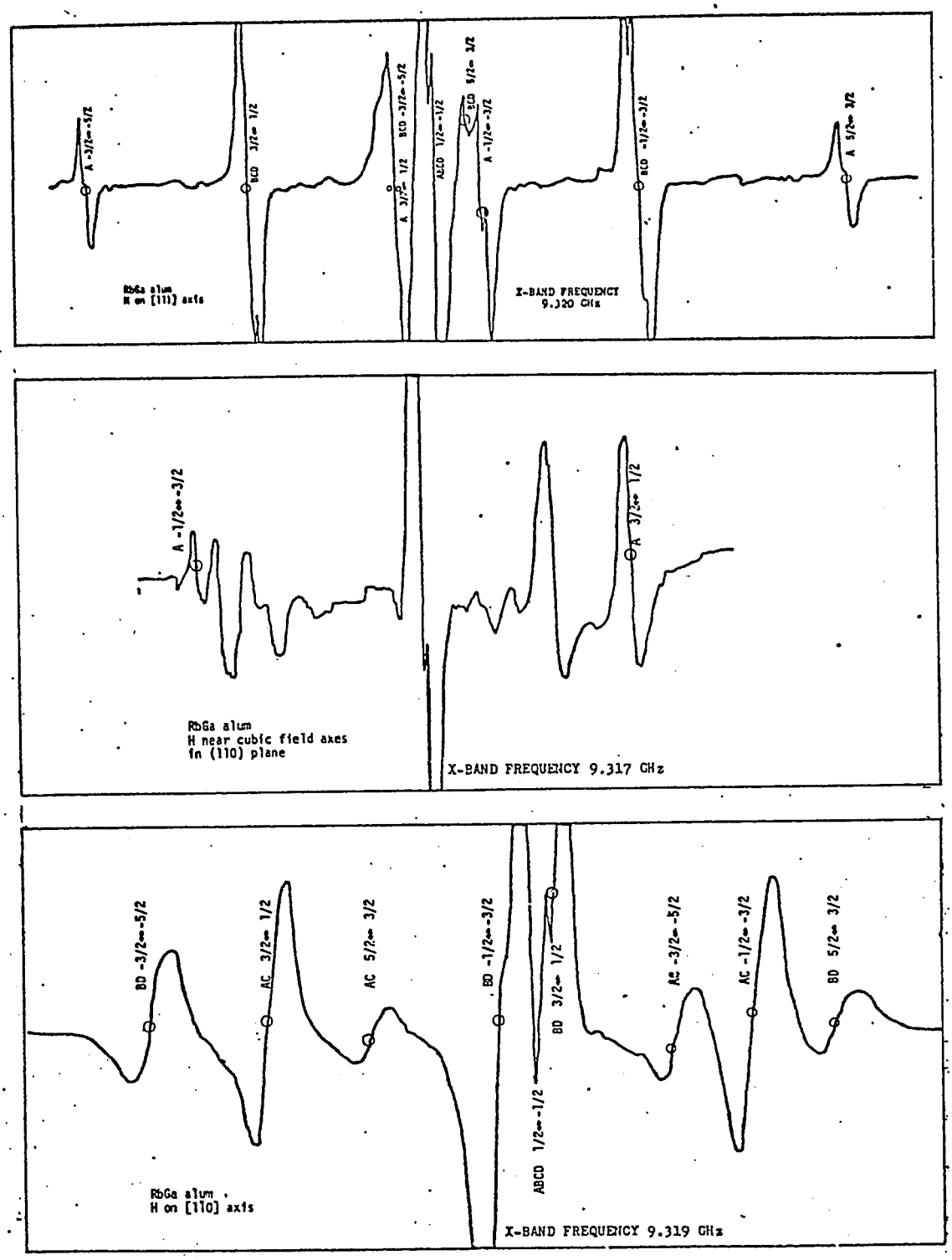

Fig. 3.5 EPR spectra for RbGa alum.

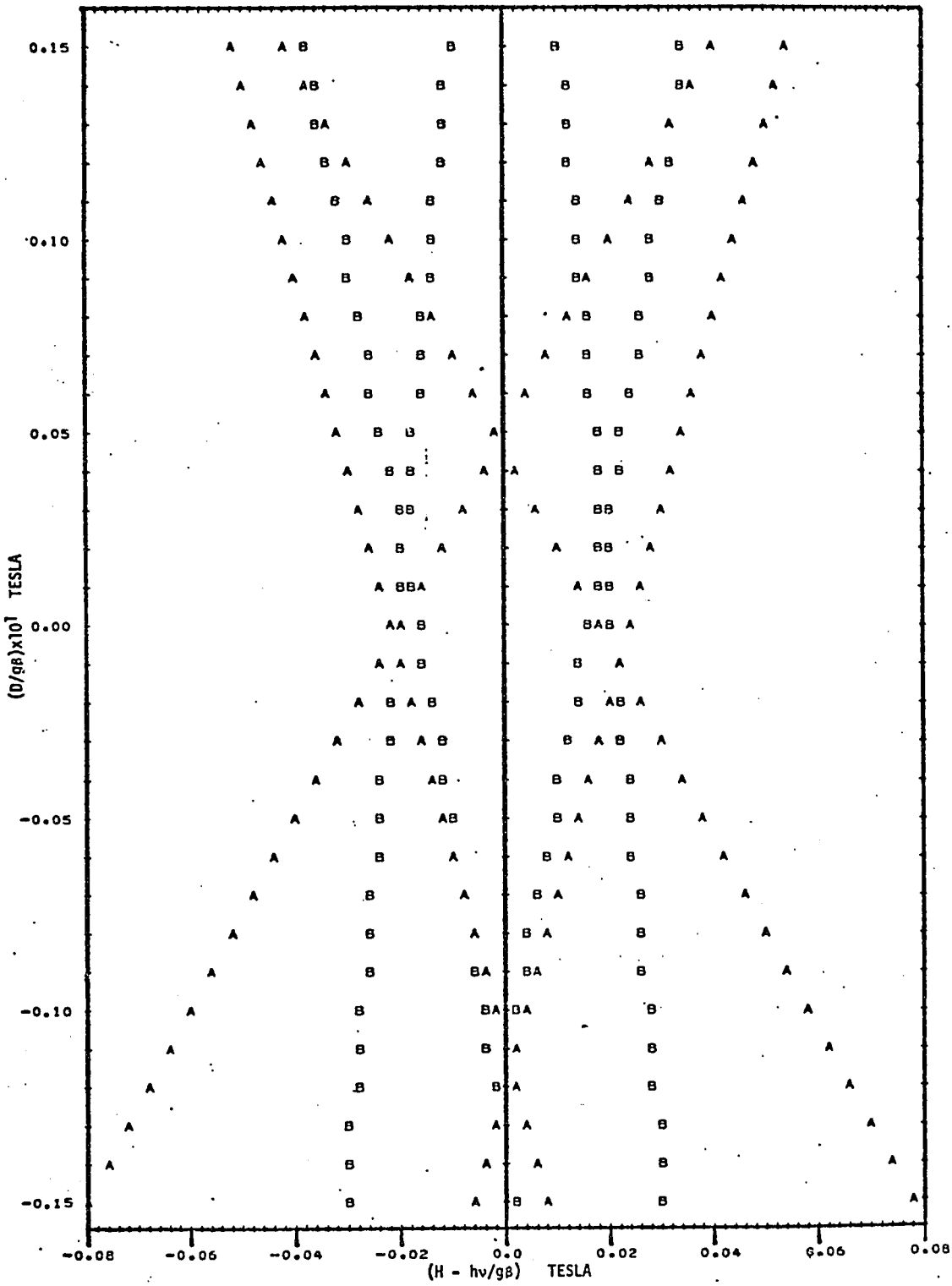

Fig. 3.6 Variation of the EPR fields vs. D in a [111] direction, with a > 0.

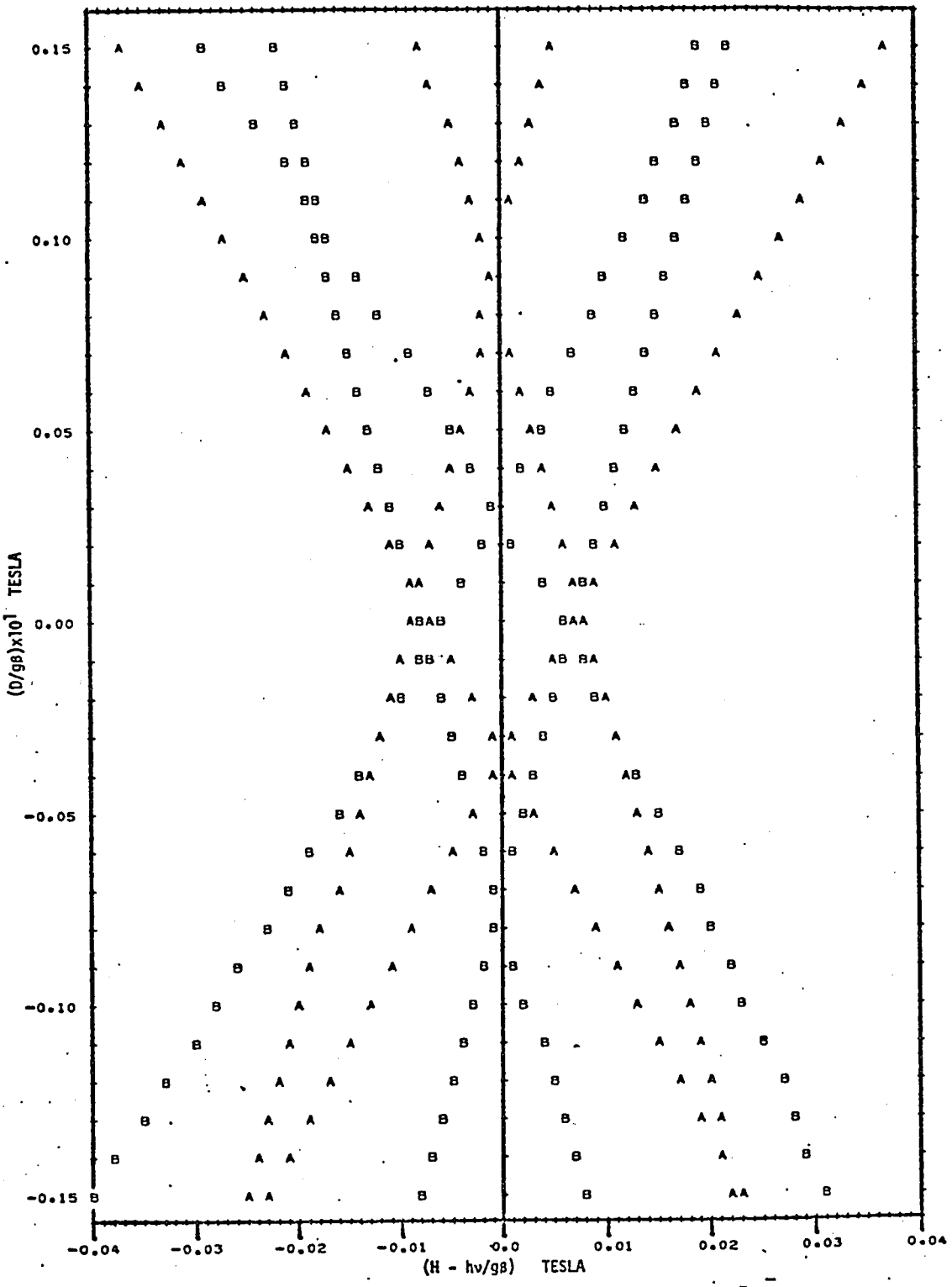

Fig. 3.7 Variation of EPR fields vs. D in a [1$\bar{1}$0] direction, with a > 0.

Table 3.3

PARAMETERS AND EPR FIELDS FOR Fe^{3+} IN $RbGa(SO_4)_2 \cdot 12\ H_2O$ AT 4.2 K

$g = 2.003$ $\quad |\alpha| = 9.5$ degrees

$a/g\beta = 0.140 \times 10^{-1}$ T $\quad D/g\beta = -0.090 \times 10^{-1}$ T $\quad F/g\beta = 0.004 \times 10^{-1}$ T

$a/hc = 133 \times 10^{-4}$ cm^{-1} $\quad D/hc = -84 \times 10^{-4}$ cm^{-1} $\quad F/hc = 4 \times 10^{-4}$ cm^{-1}

DIRECTION OF MAGNETIC FIELD H	EPR FIELDS, H, 10^{-1} T										
	OBSERVED						CALCULATED				
						SITE	$-\frac{1}{2} \rightarrow -\frac{3}{2}$	$+\frac{5}{2} \rightarrow +\frac{3}{2}$	$+\frac{1}{2} \rightarrow -\frac{1}{2}$	$-\frac{3}{2} \rightarrow -\frac{5}{2}$	$+\frac{3}{2} \rightarrow +\frac{1}{2}$
near ξηζ axes polar coordinates of H with ⟨100⟩ axes (1,9.5,-45)	2.98	3.02	3.34	3.55	3.67	A	2.98	3.03	3.33	3.59	3.67
						B	3.08	3.02	3.33	3.61	3.56
	3.06	3.09	3.14	3.52	3.64	C	3.11	3.14	3.34	3.48	3.53
						D	3.00	3.16	3.34	3.45	3.64
[111] axis	3.39	3.87	3.32	2.78	3.27	A	3.38	3.86	3.32	2.78	3.28
	3.59	3.32	3.32	3.27	3.06	BCD	3.59	3.36	3.32	3.27	3.06
[1$\bar{1}$0] axis	3.49	3.22	3.34	3.44	3.14	AC	3.49	3.21	3.32	3.44	3.14
	3.31	3.55	3.34	3.07	3.34	BD	3.30	3.54	3.34	3.07	3.34

PLOT OF EPR FIELDS FOR H NEAR ξηζ AXES

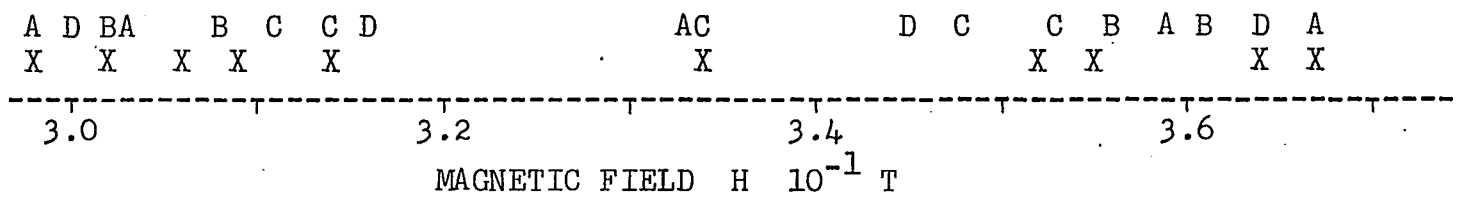

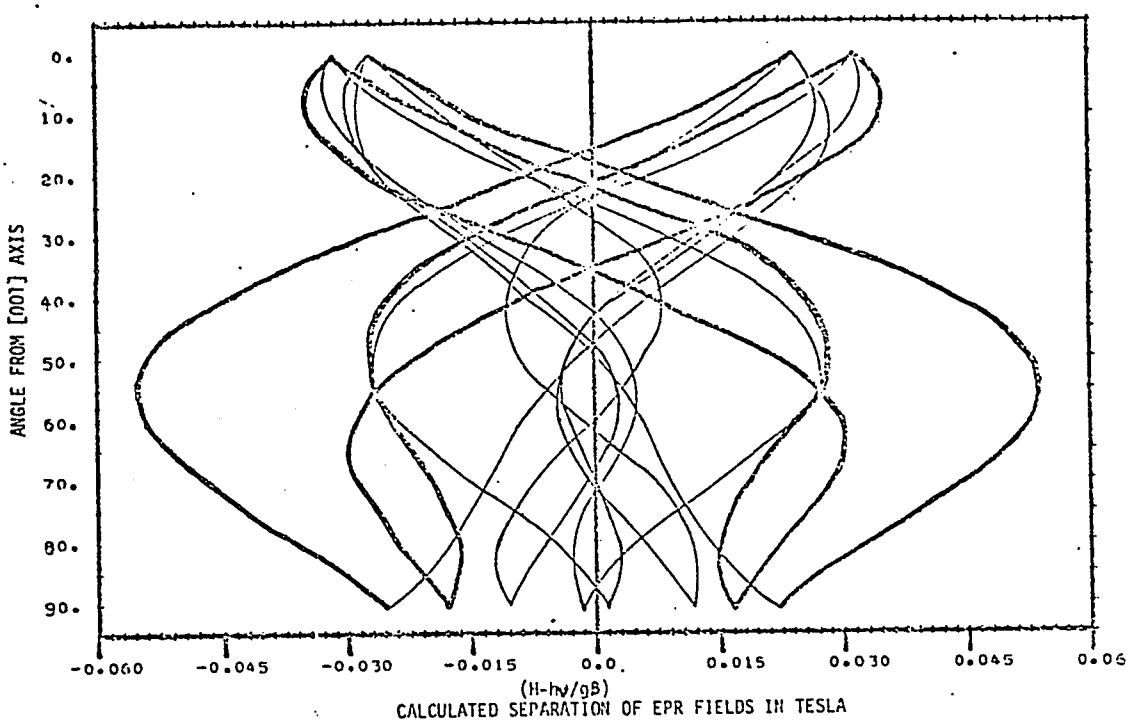

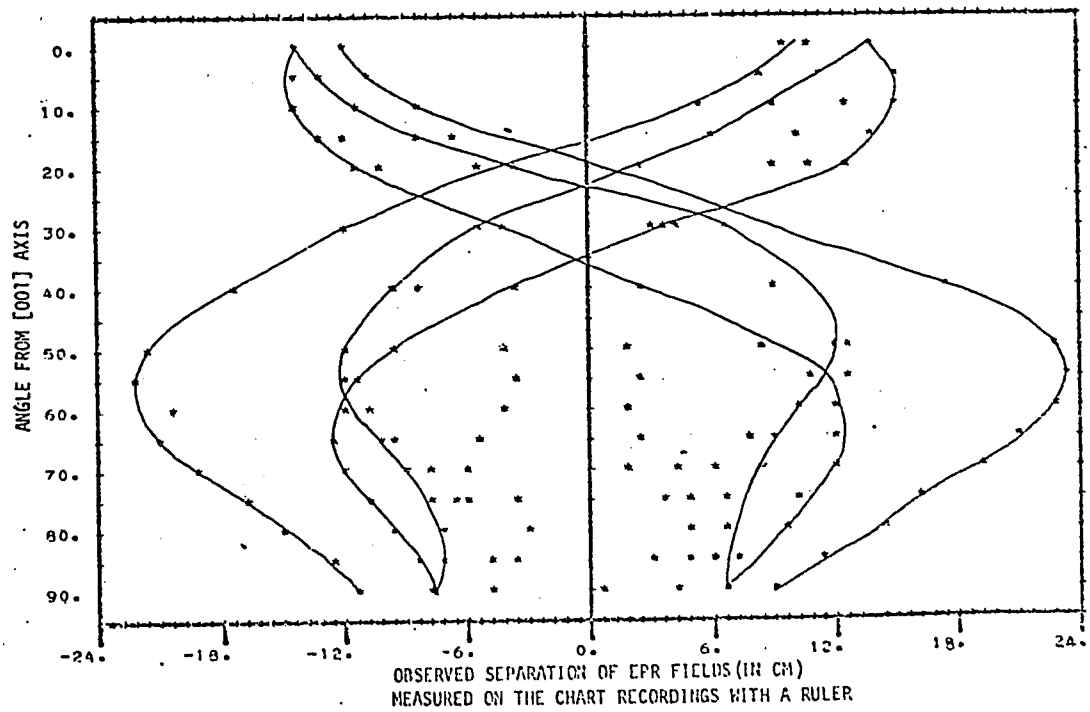

Fig. 3.8 Variation of the EPR fields in a ⟨110⟩ direction, for RbGa alum.

3.5 Error of the EPR Parameters

Since the EPR fields were fitted within 0.001 T, the error on the fine structure parameters a, D, F, is the amount by which an independent variation of a parameter from its best fit value produces a 0.001 T change in the calculated EPR fields . Thus for both alums,

$\Delta a = \pm 4 \times 10^{-4}$ cm^{-1} or $\pm$ 10 MHz,

$\Delta D = \pm 2 \times 10^{-4}$ cm^{-1} or $\pm$ 5 MHz,

$\Delta F = \pm 2 \times 10^{-4}$ cm^{-1} or $\pm$ 5 MHz,

and $\Delta g = \pm 0.003$.

CHAPTER 4

ENDOR THEORY

4.1 The Nuclear Spin Hamiltonian

Locher and Geschwind [11] used the following nuclear spin Hamiltonian in the analysis of the ENDOR spectrum of Fe^{3+} in MgO :

$$\mathcal{H}_n = [\ A - \tfrac{1}{5}(3S^2+3S-1)U\ ]\vec{S}\cdot\vec{I} - g_I\beta_N\vec{H}\cdot\vec{I}$$

$$+ U[\ S_\xi^3 + S_\eta^3 + S_\zeta^3\ ]\ . \qquad \ldots\ (1)$$

The ξ, η, and ζ directions in this equation are along the cubic axes of the MgO crystal. In alums, since the local symmetry is trigonal, these terms must be rotated to the trigonal axes.

In trigonal symmetry the allowed hyperfine and nuclear Zeeman terms are

$$AS_zI_z + B(S_xI_x + S_yI_y)$$

$$-g_I^{\parallel}\beta_N H_z I_z - g_I^{\perp}\beta_N(H_xI_x + H_yI_y)\ .$$

As in the case of the electronic g term for an S-state ion,

$$g_I^{\parallel} = g_I^{\perp} = g_I$$

within experimental error, and the nuclear Zeeman term remains $g_I \beta_N \vec{H} \cdot \vec{I}$.

The U term is rotated to the trigonal axes by the following rotation

$$\begin{pmatrix} S_\xi \\ S_\eta \\ S_\zeta \end{pmatrix} = \begin{bmatrix} -1/\sqrt{6} & 1/\sqrt{2} & 1/\sqrt{3} \\ -1/\sqrt{6} & -1/\sqrt{2} & 1/\sqrt{3} \\ 2/\sqrt{6} & 0 & 1/\sqrt{3} \end{bmatrix} \begin{pmatrix} S_x \\ S_y \\ S_z \end{pmatrix} ,$$

and similarly for I_ξ, I_η, I_ζ. Here the x axis is chosen as the projection of the ζ axis in the trigonal plane. Hence, it is found that the U term in equation (1) can be expressed in this trigonal set of axes as

$$\begin{aligned} & U_{\parallel} \left[-\tfrac{2}{3} S_z^3 I_z + \tfrac{2}{15}(3S^2+3S-1) S_z I_z \right] \\ & - U_{\perp} \left[\tfrac{1}{12}(S_-^2 S_+ + S_- S_+ S_- + S_+ S_-^2) I_+ \right. \\ & \qquad + \tfrac{1}{12}(S_+^2 S_- + S_+ S_- S_+ + S_- S_+^2) I_- \\ & \qquad \left. - \tfrac{1}{15}(3S^2+3S-1)(S_- I_+ + S_+ I_-) \right] \\ & + U'_{\parallel} \tfrac{1}{6\sqrt{2}}(S_+^3 + S_-^3) I_z + \tfrac{U'_{\perp}}{2\sqrt{2}} \left[S_- S_z S_- I_- + S_+ S_z S_+ I_+ \right] . \end{aligned}$$

$U_{\parallel} = U_{\perp} = U'_{\parallel} = U'_{\perp} = U$ for cubic symmetry. In trigonal symmetry, four independent terms are allowed by group theory considerations [12] if the nuclear and electronic spin axes coincide. Thus $U_{\parallel}$ $U_{\perp}$ $U'_{\parallel}$ $U'_{\perp}$ are chosen to represent the behaviour of a S^3I term in trigonal symmetry. The rotation of the S^3I term from the cubic to the trigonal axes was also verified directly on a computer, as described in appendix 2.

For H at an angle θ with the z axis, and the x axis taken to be along the projection of the ζ axis in the trigonal plane (Fig. 3.2), the nuclear Zeeman term $g_I\beta_N\vec{H}\cdot\vec{I}$ can be expressed as

$$g_I\beta_N[H\cos\theta I_z + H\sin\theta(I_+e^{-i(\varphi-\alpha)} + I_-e^{i(\varphi-\alpha)}\ ].$$

By expressing the nuclear spin Hamiltonian with the x axis taken to be along the projection of $\vec{H}$ in the trigonal plane, as done in chapter 3 for the EPR Hamiltonian, the following transformations are done:

$$I_+ \longrightarrow I_+e^{i(\varphi-\alpha)} \quad \text{and} \quad I_- \longrightarrow I_-e^{-i(\varphi-\alpha)},$$

and similarly for S_+ and S_- . Hence the total spin Hamiltonian with reference to the trigonal axes as just described is

$$
\begin{aligned}
\mathcal{H} = \; & g\beta H\cos\theta S_z + \tfrac{1}{2}g\beta H\sin\theta(S_+ + S_-) \\
& - \frac{a-F}{180}[35S_z^4 - 30S(S+1)S_z^2 + 25S_z^2 - 6S(S+1) + 3S^2(S+1)^2] \\
& + \frac{a\sqrt{2}}{36}[\, S_z(S_+^3 e^{i3(\varphi-\alpha)} + S_-^3 e^{-i3(\varphi-\alpha)}) \\
& \qquad + (S_+^3 e^{i3(\varphi-\alpha)} + S_-^3 e^{-i3(\varphi-\alpha)})S_z \,] \\
& + D[\, S_z^2 - \tfrac{1}{3}S(S+1) \,] \\
& - g_I\beta_N H\cos\theta I_z - \tfrac{1}{2}g_I\beta_N H\sin\theta(I_+ + I_-) \\
& + [\, A + \frac{2}{15}(3S^2 + 3S - 1)U_{\parallel} \,]S_zI_z \\
& + [\, B + \frac{2}{15}(3S^2 + 3S - 1)U_{\perp} \,]\tfrac{1}{2}(S_-I_+ + S_+I_-) \\
& - U_{\parallel}[\, \tfrac{2}{3}S_z^3I_z \,] \\
& - U_{\perp}\tfrac{1}{12}[(S_-^2S_+ + S_-S_+S_- + S_+S_-^2)I_+ \\
& \qquad + (S_+^2S_- + S_+S_-S_+ + S_-S_+^2)I_- \,] \\
& + U'_{\parallel}\tfrac{1}{6\sqrt{2}}[\, S_+^3 e^{i3(\varphi-\alpha)} + S_-^3 e^{-i3(\varphi-\alpha)} \,]I_z \\
& + U'_{\perp}\tfrac{1}{2\sqrt{2}}[\, S_+S_zS_+I_+e^{i3(\varphi-\alpha)} + S_-S_zS_-I_-e^{-i3(\varphi-\alpha)} \,] .
\end{aligned}
$$

With the spin functions $|M,m\rangle$ as basis functions, the spin Hamiltonian is written in Hermitian form as $\langle M',m'|\mathcal{H}|M,m\rangle$, where M and m are the electronic and nuclear spin magnetic quantum numbers. Most of the matrix elements for the spin Hamiltonian can be found in Low's book [13]. For the S^3I term in trigonal form some of the non-zero matrix elements are, for $I=\frac{1}{2}$,

$$\langle M,m|S_z^3 I_z|M,m\rangle = M^3 m \ ,$$

$$\langle M-1,\tfrac{1}{2}|(S_-^2S_+ + S_-S_+S_- + S_+S_-^2)I_+|M,-\tfrac{1}{2}\rangle = [3(S+M)(S-M+1)-2][(S+M)(S-M+1)]^{\frac{1}{2}} \ ,$$

$$\langle M-2,-\tfrac{1}{2}|S_-S_zS_-I_-|M,\tfrac{1}{2}\rangle = (M-1)\left[\frac{(S+M)!(S-M+2)!}{(S-M)!(S+M-2)!}\right]^{\frac{1}{2}} \ ,$$

$$\langle M-3,m|S_-^3 I_z|M,m\rangle = m\left[\frac{(S+M)!(S-M+3)!}{(S-M)!(S+M-3)!}\right]^{\frac{1}{2}} \ .$$

The elements of the spin Hamiltonian matrix $\mathcal{H}_{ij}$ are written in the following order

$$i = \langle 5/2,\tfrac{1}{2}|,\ \langle 5/2,-\tfrac{1}{2}|,\ \langle 3/2,\tfrac{1}{2}|,\ \ldots\langle -5/2,-\tfrac{1}{2}|$$

$$j = |5/2,\tfrac{1}{2}\rangle,\ |5/2,-\tfrac{1}{2}\rangle,\ |3/2,\tfrac{1}{2}\rangle,\ \ldots|-5/2,-\tfrac{1}{2}\rangle.$$

In Table 4.1 are given the non-zero matrix elements on and below the diagonal elements.

$\langle M-3,m\|$	$\langle M-2,m-1\|$ $\langle M-3,m+1\|$	$\langle M-1,m\|$	$\langle M\ \ ,m-1\|$ $\langle M-1,m+1\|$	$\langle M,m\ \|$	$\|M,\ m\rangle$
$\sqrt{5}(\frac{2a}{3}+\frac{U_\parallel}{2})e^{-i3(\varphi-\alpha)}$	$\frac{3}{2}\sqrt{5}U_\perp e^{-i3(\varphi-\alpha)}$	$\frac{\sqrt{5}}{2}g\beta H\sin\theta$	$-\frac{1}{2}g_I\beta_N H\sin\theta$	$(5g\beta-g_I\beta_N)H\cos\theta/2$ $-(a-F-10D)/3$ $+5A/4-U_\parallel$	$\|\frac{5}{2},\frac{1}{2}\rangle$
$\sqrt{5}(\frac{2a}{3}-\frac{U_\parallel}{2})e^{-i3(\varphi-\alpha)}$		$\frac{\sqrt{5}}{2}g\beta H\sin\theta$	$\sqrt{5}(\frac{B}{2}+\frac{3U_\perp}{5})$	$(5g\beta+g_I\beta_N)H\cos\theta/2$ $-(a-F-10D)/3$ $-5A/4+U_\parallel$	$\|\frac{5}{2},-\frac{1}{2}\rangle$
$\sqrt{2}U_\parallel e^{-i3(\varphi-\alpha)}$	$\frac{3}{2}U_\perp e^{-i3(\varphi-\alpha)}$	$\sqrt{2}g\beta H\sin\theta$	$-\frac{1}{2}g_I\beta_N H\sin\theta$	$(3g\beta-g_I\beta_N)H\cos\theta/2$ $+(a-F)-2D/3$ $+3A/4+7U_\parallel/5$	$\|\frac{3}{2},\frac{1}{2}\rangle$
$-\sqrt{2}U_\parallel e^{-i3(\varphi-\alpha)}$		$\sqrt{2}g\beta H\sin\theta$	$\sqrt{2}(B-\frac{3U_\perp}{10})$	$(3g\beta+g_I\beta_N)H\cos\theta/2$ $+(a-F)-2D/3$ $-3A/4-7U_\parallel/5$	$\|\frac{3}{2},-\frac{1}{2}\rangle$
$-\sqrt{5}(\frac{2a}{3}-\frac{U_\parallel}{2})e^{-i3(\varphi-\alpha)}$	$-\frac{3}{2}\sqrt{5}U_\perp e^{-i3(\varphi-\alpha)}$	$\frac{3}{2}g\beta H\sin\theta$	$-\frac{1}{2}g_I\beta_N H\sin\theta$	$(g\beta-g_I\beta_N)H\cos\theta/2$ $-2(a-F+4D)/3$ $+A/4+4U_\parallel/5$	$\|\frac{1}{2},\frac{1}{2}\rangle$
$-\sqrt{5}(\frac{2a}{3}+\frac{U_\parallel}{2})e^{-i3(\varphi-\alpha)}$		$\frac{3}{2}g\beta H\sin\theta$	$\frac{3}{2}B-\frac{6U_\perp}{5}$	$(g\beta+g_I\beta_N)H\cos\theta/2$ $-2(a-F+4D)/3$ $-A/4-4U_\parallel/5$	$\|\frac{1}{2},-\frac{1}{2}\rangle$
	$-\frac{3}{2}\sqrt{5}U_\perp e^{-i3(\varphi-\alpha)}$	$\sqrt{2}g\beta H\sin\theta$	$-\frac{1}{2}g_I\beta_N H\sin\theta$	$(-g\beta-g_I\beta_N)H\cos\theta/2$ $-2(a-F+4D)/3$ $-A/4-4U_\parallel/5$	$\|-\frac{1}{2},\frac{1}{2}\rangle$
		$\sqrt{2}g\beta H\sin\theta$	$\sqrt{2}(B-\frac{3U_\perp}{10})$	$(-g\beta+g_I\beta_N)H\cos\theta/2$ $-2(a-F+4D)/3$ $+A/4+4U_\parallel/5$	$\|-\frac{1}{2},-\frac{1}{2}\rangle$
		$\frac{\sqrt{5}}{2}g\beta H\sin\theta$	$-\frac{1}{2}g_I\beta_N H\sin\theta$	$(-3g\beta-g_I\beta_N)H\cos\theta/2$ $+(a-F)-2D/3$ $-3A/4-7U_\parallel/5$	$\|-\frac{3}{2},\frac{1}{2}\rangle$
		$\frac{\sqrt{5}}{2}g\beta H\sin\theta$	$\sqrt{5}(\frac{B}{2}+\frac{3U_\perp}{5})$	$(-3g\beta+g_I\beta_N)H\cos\theta/2$ $+(a-F)-2D/3$ $+3A/4+7U_\parallel/5$	$\|-\frac{3}{2},-\frac{1}{2}\rangle$
			$-\frac{1}{2}g_I\beta_N H\sin\theta$	$(-5g\beta-g_I\beta_N)H\cos\theta/2$ $-(a-F-10D)/3$ $-5A/4+U_\parallel$	$\|-\frac{5}{2},\frac{1}{2}\rangle$
				$(-5g\beta+g_I\beta_N)H\cos\theta/2$ $-(a-F-10D)/3$ $+5A/4-U_\parallel$	$\|-\frac{5}{2},-\frac{1}{2}\rangle$

Table 4.1 Non zero elements of the spin Hamiltonian matrix.

4.2 ENDOR Transitions to First Order in Perturbation Theory

The hyperfine energy levels are first analyzed to first order in perturbation theory, neglecting the fine structure terms which have little effect on the hyperfine levels. With the magnetic field in the xz plane the Hamiltonian can be written as

$$\begin{aligned}\mathcal{H} = {} & g\beta H(S_z\cos\theta + S_x\sin\theta) - g_I\beta_N H(I_z\cos\theta + I_x\sin\theta) \\ & + A'S_zI_z + B'(S_xI_x + S_yI_y) - \tfrac{2}{3}U_{\parallel}S_z^3I_z \\ & - \frac{U_\perp}{12}[(S_-^2S_+ + S_-S_+S_- + S_+S_-^2)I_+ + (S_+^2S_- + S_+S_-S_+ + S_-S_+^2)I_-] \\ & + \frac{U_\parallel'}{6\sqrt{2}}[\,S_+^3e^{i3\rho} + S_-^3e^{-i3\rho}\,]I_z \\ & + \frac{U_\perp'}{2\sqrt{2}}[\,S_+S_z\,S_+I_+e^{i3\rho} + S_-S_zS_-I_-e^{-i3\rho}\,] \quad ,\end{aligned}$$

where

$$A' = A + 2U_{\parallel}(3S^2 + 3S - 1)/15 \quad ,$$

$$B' = B + 2U_{\perp}(3S^2 + 3S - 1)/15 \quad ,$$

$$\rho = (\varphi - \alpha) \quad .$$

The electronic Zeeman term $g\beta\vec{H}\cdot\vec{S}$ is diagonalized first by changing to a new set of axes for $\vec{S}$ which are rotated from the original set by an angle θ about

the y axis. Hence,

$$\begin{pmatrix} S_+ \\ S_- \\ S_z \end{pmatrix} = \begin{bmatrix} a^2 & -b^2 & 2ab \\ -b^2 & a^2 & 2ab \\ -ab & -ab & (a^2-b^2) \end{bmatrix} \begin{pmatrix} S'_+ \\ S'_- \\ S'_z \end{pmatrix} ,$$

where $a = \cos(\theta/2)$ and $b = \sin(\theta/2)$.

This transformation diagonalizes the Zeeman term to $g\beta HS'_z$. To diagonalize the SI term the $\vec{I}$ axes must be rotated by an angle Ψ about the y axis [14], so that

$$\tan\Psi = \frac{B'}{A'} \tan\theta$$

and

$$A'S_zI_z + \frac{1}{2}B'(S_-I_+ + S_+I_-) = KS'_zI'_z \quad ,$$

where

$$K^2 = (A'\cos\theta)^2 + (B'\sin\theta)^2 .$$

However, in our case, $B' \cong A'$, and so Ψ is put equal to θ. With the rotation matrix for the $\vec{I}$ axes being the same as the $\vec{S}$ axes, then we have

$$g_I\beta_N\vec{H}\cdot\vec{I} = g_I\beta_N H\, I'_z .$$

For the first order contribution of the S^3I term, the expressions for S_+, S_-, S_z and I_+, I_-, I_z in terms of S'_+, S'_-, S'_z and I'_+, I'_-, I'_z are substi-

tuted in the Hamiltonian and the resulting cubic expansion is carried out. Then the six possible combinations of the diagonal term $S_z'S_+'S_-'I_z'$ are collected and simplified by means of commutation relations to terms involving $S_z'^3I_z'$ and $S'I_z'$, as presented in appendix 3. Finally, dropping the primes, the spin Hamiltonian to first order in perturbation theory becomes

$$\mathcal{H} = g\beta HS_z - g_I\beta_N HI_z + KS_zI_z$$
$$- \frac{U_\parallel}{3}\cos^2\theta\left[\left(5S_z^2-\frac{101}{4}\right)\cos^2\theta - \left(3S_z^2-\frac{101}{4}\right) \right]S_zI_z$$
$$- \frac{U_\perp}{12}\sin^2\theta\left[3\left(5S_z^2-\frac{101}{4}\right)\sin^2\theta -4\left(3S_z^2-\frac{101}{4}\right) \right]S_zI_z$$
$$+ \frac{1}{6\sqrt{2}}(U_\parallel' + 3U_\perp')\sin^3\theta\cos\theta\cos3\rho\left[5S_z^2-\frac{101}{4} \right]S_zI_z \quad .$$

The energy of the level (M,m) will be

$$\langle M,m|\mathcal{H}|M,m\rangle = \mathcal{H}_{M,m} \quad .$$

The ENDOR transition $(M,m)\rightarrow(M,m-1)$ will require a quantum of energy

$$h\upsilon = |\ \mathcal{H}_{M,m} - \mathcal{H}_{M,m-1}\ | \quad .$$

For frequencies at a constant field this leads to

$$\frac{h\upsilon(M) + h\upsilon(-M)}{2|M|} =$$

$$= | K - \frac{U_{11}}{3}\cos^2\theta[(5M^2-\frac{101}{4})\cos^2\theta - (3M^2- \frac{101}{4})]$$

$$- \frac{U_{\perp}}{12}\sin^2\theta[3(5M^2-\frac{101}{4})\sin^2\theta -4(3M^2- \frac{101}{4})]$$

$$+ \frac{1}{6\sqrt{2}}(U'_{11} + 3U'_{\perp})\sin^3\theta\cos\theta\cos3\rho(5M^2- \frac{101}{4}) |.$$

The same procedure is applied to calculate the first order contribution of the a term in section 3.3, which gives

$$p = -q/12 + \frac{1}{3}5\sqrt{2}\sin^3\theta\cos\theta\cos3\rho .$$

CHAPTER 5

ENDOR RESULTS

5.1 Introduction

ENDOR measurements on $^{57}Fe^{3+}$ in RbAl and RbGa alums were performed with the magnetic field $\vec{H}$ parallel to the [111] direction and also with $\vec{H}$ near the cubic field axis ζ_A . For a given paramagnetic site, six ENDOR lines (M = 5/2, 3/2, ...-5/2) can be observed. The corresponding frequencies are denoted by $\upsilon(M)$. These frequencies depend upon the magnitude and direction of the magnetic field.

In alums there are four paramagnetic sites per unit cell. Thus for $\vec{H}$ in a general direction of the crystal, such as near the cubic field axes, 4 $\upsilon(M)$ lines should be observed. These are denoted by υ_A, υ_B, υ_C and υ_D. When $\vec{H}$ is parallel to the [111] direction sites BCD are equivalent, as shown in Table 5.1. In this direction only 2 $\upsilon(M)$ lines should be observed, υ_A and υ_{BCD}.

Table 5.1 Angles in the spin Hamiltonian for $\vec{H}$ parallel to the [111] direction of the crystal.

SITE		A	B	C	D
TRIGONAL AXIS		111	$\bar{1}11$	$\bar{1}\bar{1}1$	$1\bar{1}1$
THETA	θ	0	70.5	109.5	70.5
PHI	φ	0	60	0	-60
ALPHA	α	9.5	-9.5	9.5	-9.5

The hyperfine parameters are obtained from the frequency measurements. From the first order perturbation theory equations developed in section 4.2, the first approximation to the parameters can be found. For more accurate values the spin Hamiltonian matrix must be diagonalized exactly. This diagonalization was performed on a computer with the program given in appendix 4. The eigenvalues obtained were accurate to five significant figures for any direction of the magnetic field. Using perturbation theory the calculated frequencies were accurate to only two significant figures along a ⟨111⟩ direction.

5.2 ENDOR of RbAl Alum

Some ENDOR spectra obtained for RbAl alum are shown in Fig. 5.1 for $\vec{H}$ along the [111] direction and in Fig. 5.2 for $\vec{H}$ near the ζ_A axis. The $\upsilon(\pm 5/2)$ frequencies were large and easy to measure for most EPR lines. For $\vec{H}$ along the [111] direction the $\upsilon_A(\pm 5/2)$ frequencies were often masked by the $\upsilon_B(\pm 5/2)$ frequencies. Less accuracy was consequently obtained

in the measurement of these lines. Only one point was identified accurately where the $\upsilon_A(5/2)$ line occured alone. This was on the A $5/2 \rightarrow 3/2$ EPR line. The $\upsilon(\pm 3/2)$ frequencies were, in general, much smaller in intensity than the $\upsilon(\pm 5/2)$ frequencies. Less accuracy was consequently obtained because the smallness of the line leads to a larger error in locating its central position.

Linewidths for all frequencies were 0.05 to 0.1 MHz, which is about the difference between the 2 $\upsilon(M)$ lines of the two sites for $\vec{H}$ along the [111] direction. When two frequencies overlap, the center of the first derivative of the absorption curves shift. This introduces a systematic error in the measurement of these lines. The accuracy of the ENDOR frequencies was thus reduced to a maximun of 0.02 MHz.

The $\upsilon(\pm 1/2)$ transitions could not be identified since too many lines overlapped in their region of the spectrum. Thus the measurements taken in the 15-17 MHz range were not utilized in the fitting process.

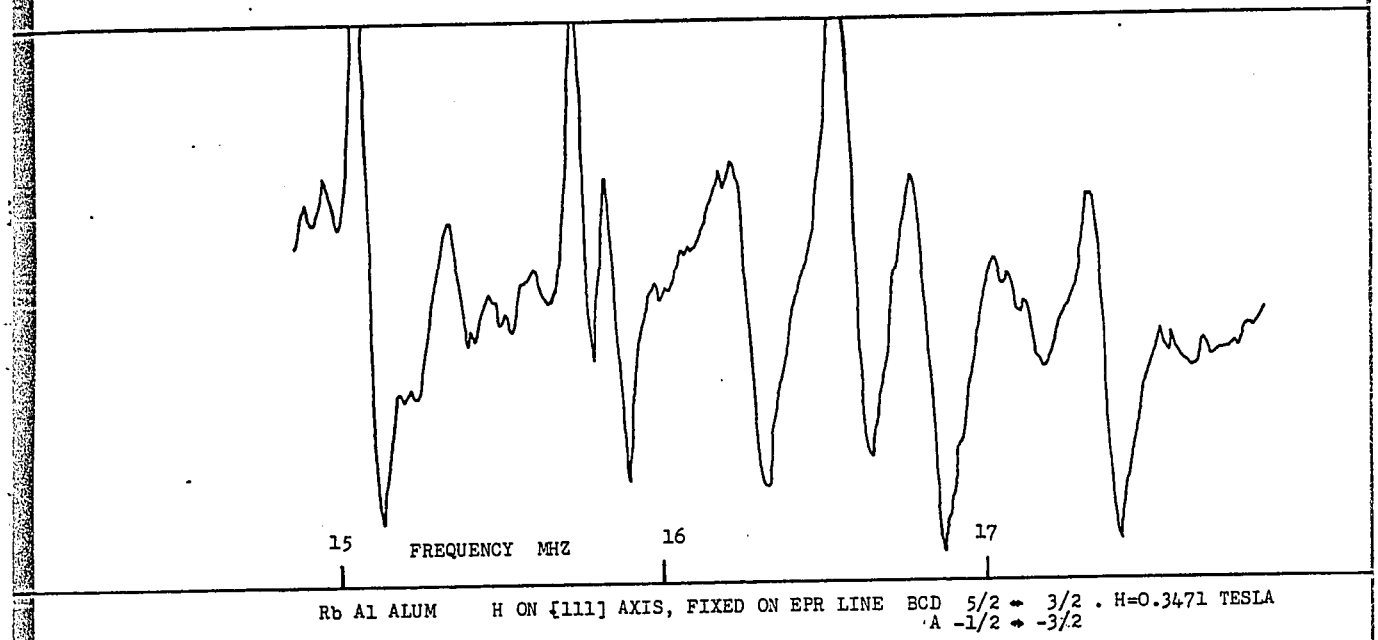

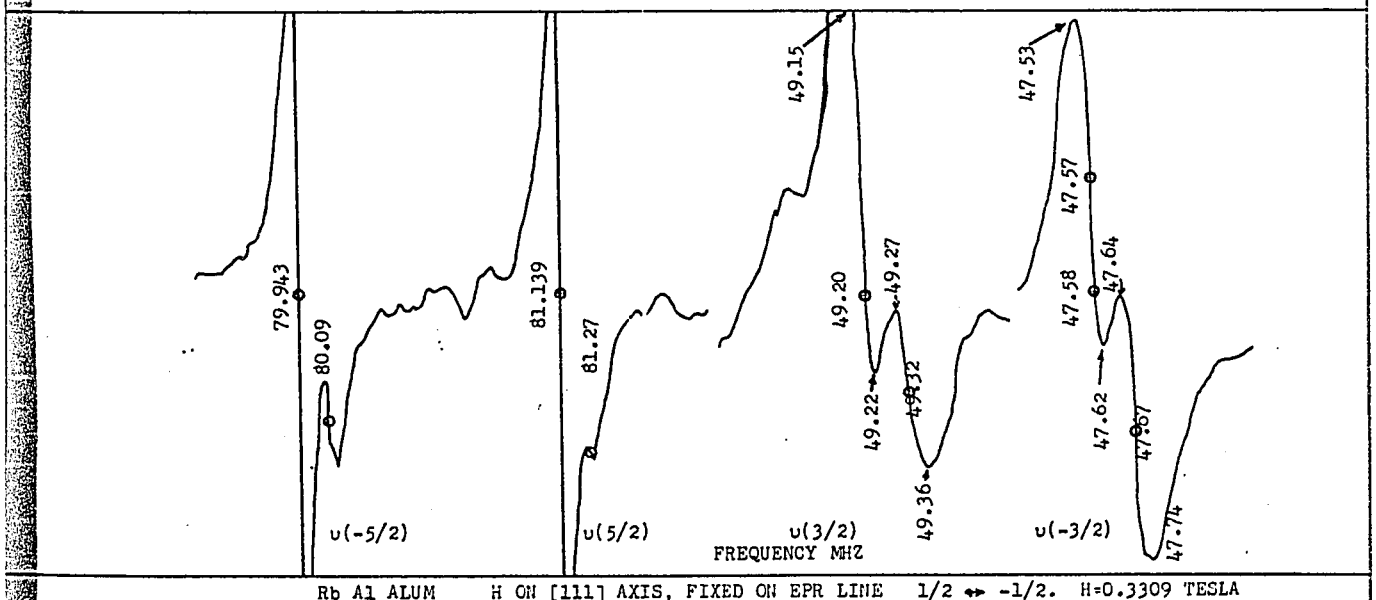

Fig. 5.1 ENDOR spectra of RbAl alum.

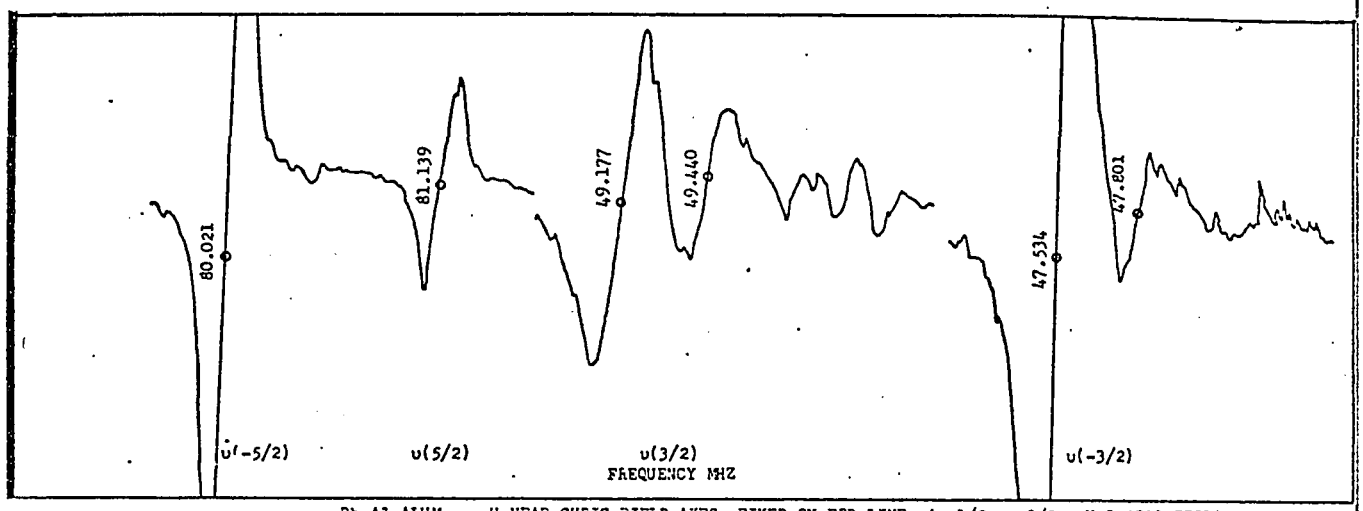

Rb Al ALUM H NEAR CUBIC FIELD AXES, FIXED ON EPR LINE A -1/2 ⇔ -3/2. H=0.2971 TESLA

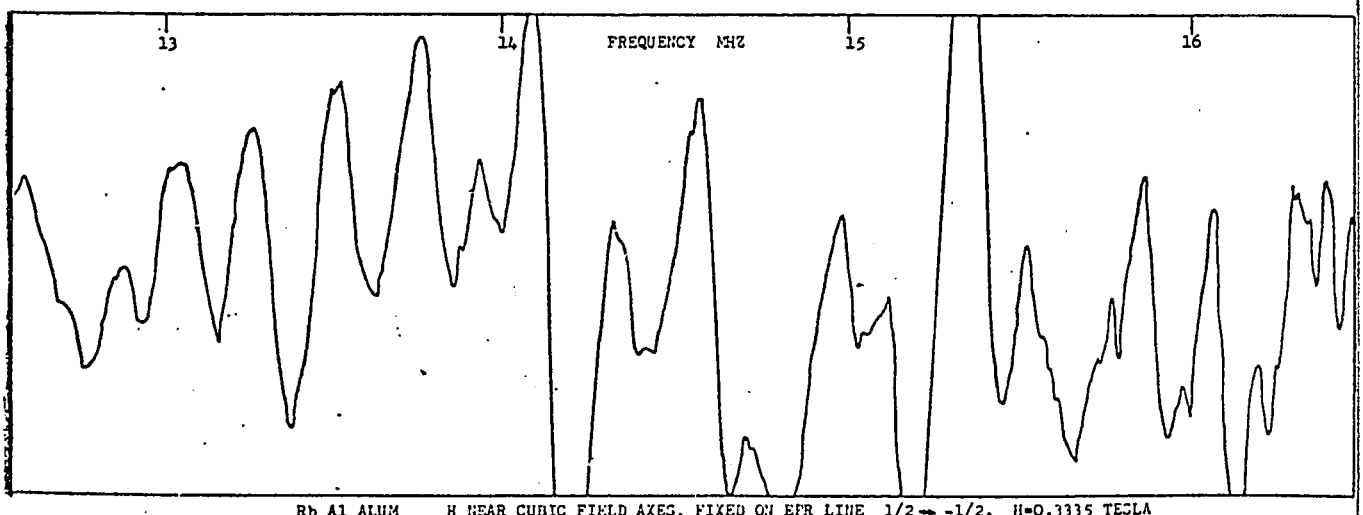

Rb Al ALUM H NEAR CUBIC FIELD AXES, FIXED ON EPR LINE 1/2 ⇔ -1/2. H=0.3335 TESLA

Fig. 5.2 ENDOR spectra of RbAl alum.

5.3 Parameters for RbAl Alum

For $^{57}Fe^{3+}$ in MgO, Locher and Geschwind [11] found

$$A/h = -30.176 \text{ MHz} \quad \text{and} \quad U/h = -0.0057 \text{ MHz} .$$

For trigonal symmetry, $U_{\parallel}$ $U_{\perp}$ $U'_{\parallel}$ $U'_{\perp}$ will be of the same order as U. A trigonal distortion should only affect the $U_{\parallel}$ parameter, the $U_{\perp}$ $U'_{\parallel}$ $U'_{\perp}$ being too small to distinguish between them. Hence we have

$$U'_{\parallel} = U'_{\perp} = U_{\perp} ,$$

and so the five parameters A B $U_{\parallel}$ $U_{\perp}$ g_I , along with the fine structure terms, should describe the whole ENDOR spectrum.

For $\vec{H}$ parallel to the [111] crystal direction , first order perturbation theory gives

$$\frac{h\upsilon_A(M) + h\upsilon_A(-M)}{2|M|} = | A' - \frac{2}{3}M^2 U_{\parallel} | .$$

The two equations of M = 5/2, 3/2 give

$$A'/h = -32.45 \text{ MHz} \quad \text{and} \quad U_{\parallel}/h = -0.03 \text{ MHz} .$$

From the perturbation equation of site B for $\vec{H}$ on the [111] axis, we have

$$B'/h = -32.26 \text{ MHz} \quad \text{and} \quad U_{\perp}/h = -0.03 \text{ MHz} .$$

From the perturbation equation for $\vec{H}$ near the cubic

field axes we have

$B'/h = -32.17$ MHz and $U_{\perp}/h = 0.0$ MHz .

These values are used as the starting parameters for the exact diagonalization of the spin Hamiltonian.

The υ_A lines for $\vec{H}$ along the [111] direction were first fitted by varying the parameters A, $U_{\parallel}$, and g_I. The initial value for g_I was taken to be the same as the one given by Locher and Geschwind [11] in their work on MgO. With these parameters determined, then the υ_B lines for $\vec{H}$ along the [111] direction, and the frequencies for $\vec{H}$ near the cubic field axes, were fitted. The variation of the parameters was done using the condition imposed on these parameters by the first order perturbation theory equations.

Experimentally, the magnetic field orientation for $\vec{H}$ near the cubic field axes was measured as (1,9.5,-45). With this orientation only the $\upsilon_A(\pm 5/2)$ lines could be fitted, no matter how the parameters were chosen. Misalignment of a few degrees for $\vec{H}$ was found to affect the $\upsilon(\pm 3/2)$ lines considerably. A misorientation of 1 degree produced

a change in the $\upsilon(\pm 3/2)$ eigenvalues by as much as 0.03 MHz, but with no change for the $\upsilon(\pm 5/2)$ frequencies. Hence for best fit the orientation of the magnetic field was taken to be (1, 10.5,-47). The observed and calculated frequencies for both directions are plotted in Figs. 5.3 and 5.4, and are tabulated in Tables 5.2 and 5.3.

The spin Hamiltonian parameters for the ENDOR of Fe^{3+} in $RbAl(SO_4)_2 \cdot 12H_2O$ are

$g = 2.003$

$a/h = 398$ MHz

$D/h = -93$ MHz

$F/h = 11$ MHz

$g_I = 0.180$

$A'/h = -32.370$ MHz

$B'/h = -32.240$ MHz

$U_{\parallel}/h = -0.021$ MHz

$U_{\perp}/h = -0.004$ MHz

ALPHA $\alpha = 9.5$ degrees .

From these, the values of A and B are

$A/ = -32.299$ MHz

$B/h = -32.227$ MHz .

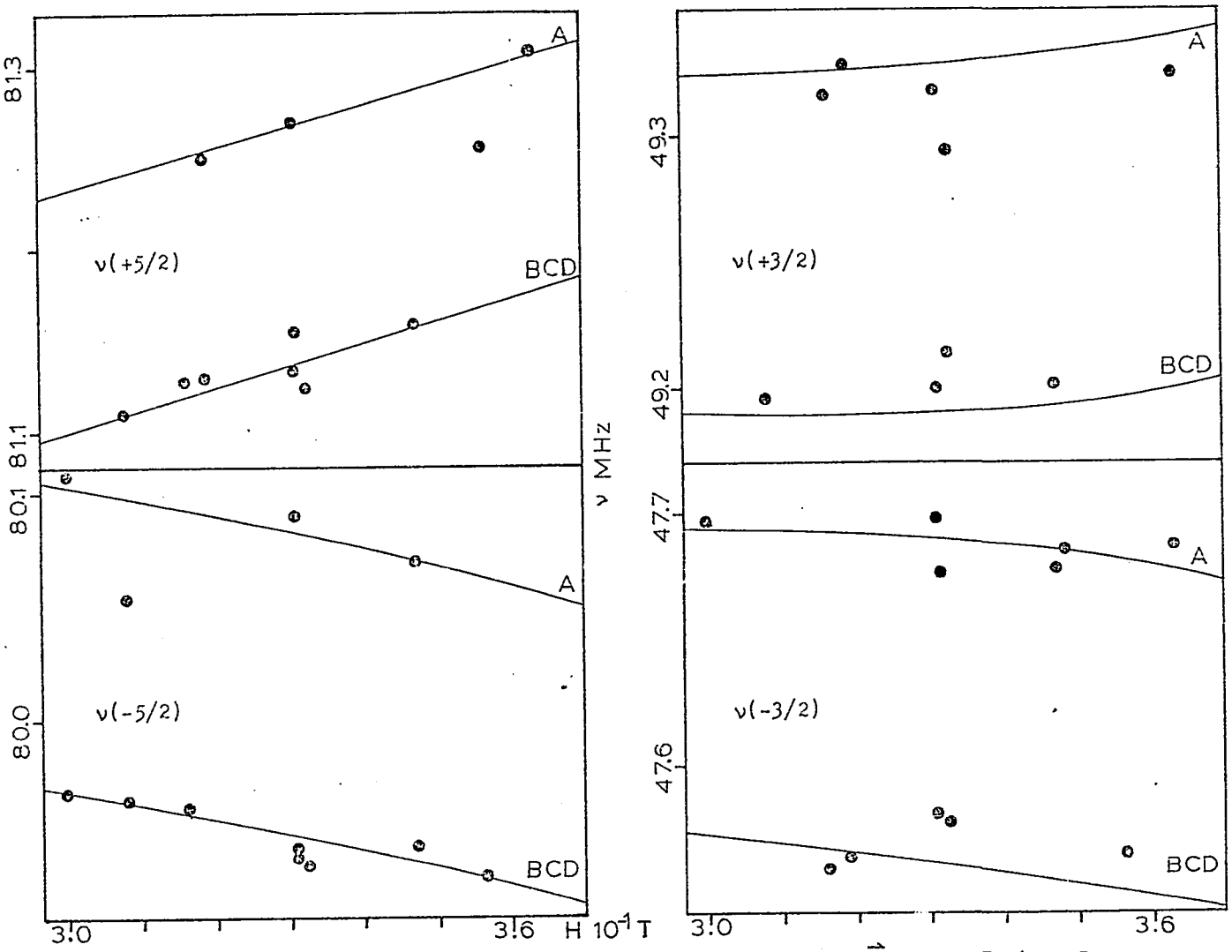

Fig. 5.3 ENDOR frequencies υ vs. the magnetic field $\vec{H}$, for RbAl alum, with $\vec{H}$ along the [111] direction.

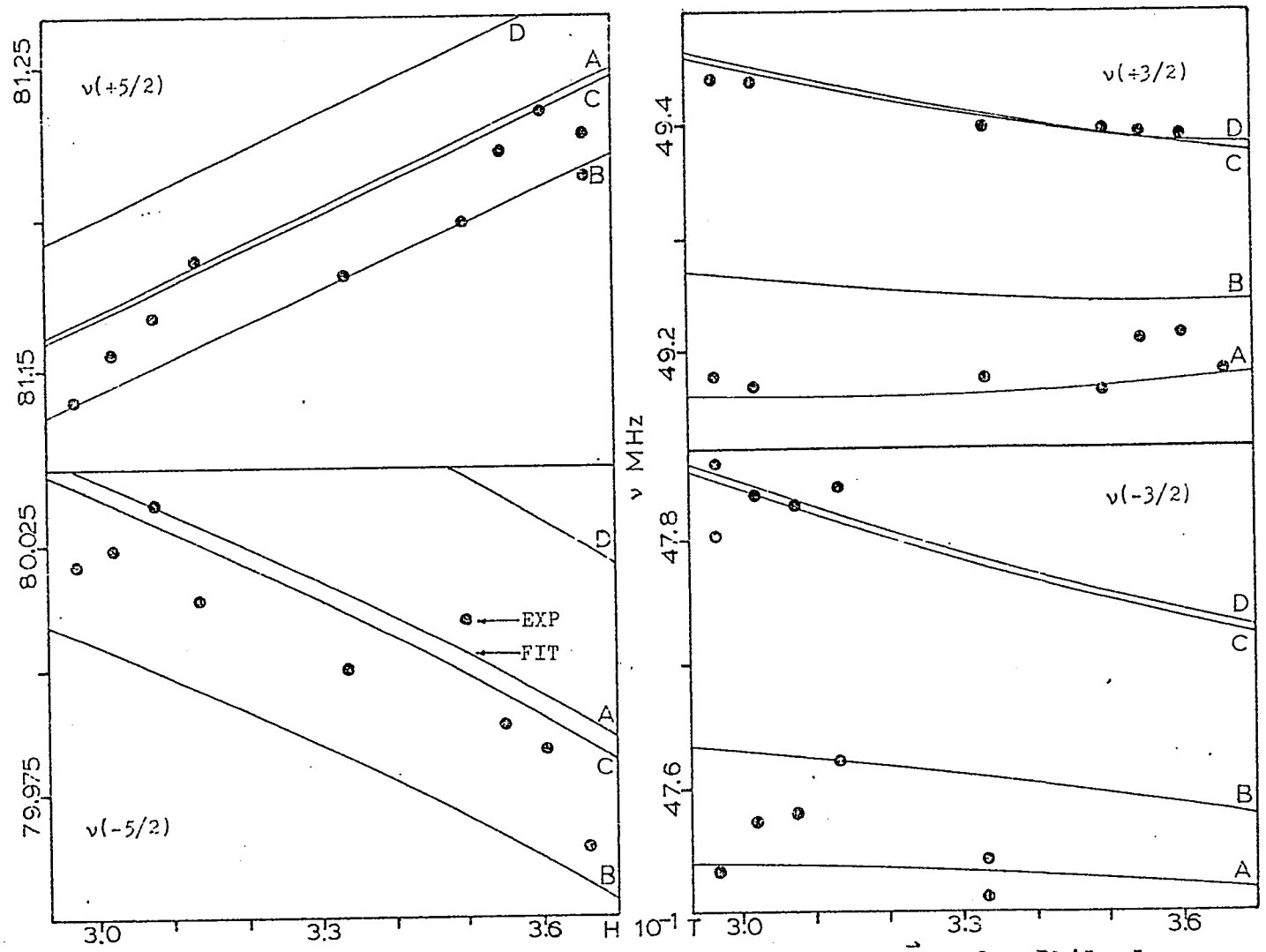

Fig. 5.4 ENDOR frequencies υ vs. the magnetic field $\vec{H}$, for RbAl alum, with $\vec{H}$ near the ζ_A axis.

Table 5.2 ENDOR frequencies for RbAl alum. H on [111] axis.

EPR FIELD 10^{-1} T	ENDOR FREQUENCY MHz OBSERVED			CALCULATED A	CALCULATED BCD
2.998	80.107			80.102	
A $-\frac{3}{2} \rightarrow -\frac{5}{2}$	47.697			47.693	
	15.40	16.16	16.33	15.18	15.29
	17.01			17.05	17.07
3.079	81.110				81.111
B $+\frac{3}{2} \rightarrow +\frac{1}{2}$	80.053	79.964		80.10	79.963
	49.196				49.189
	15.63	16.26		15.18	15.28
3.163	81.128				81.120
A $+\frac{3}{2} \rightarrow +\frac{1}{2}$	79.961				79.958
	49.320			49.325	
	47.558				47.567
	16.64	16.91	17.17	17.06	17.07
3.188	81.251	81.130		81.255	81.123
	79.956				79.956
B $-\frac{3}{2} \rightarrow -\frac{5}{2}$	49.328			49.325	
	47.563				47.566
	15.92	17.01	17.49	17.06	17.06
3.309	81.27	81.134		81.269	81.138
$+\frac{1}{2} \rightarrow -\frac{1}{2}$	80.09	79.943		80.081	79.948
	49.318	49.200		49.328	49.191
	47.698	47.580		47.689	47.56
3.313	81.156	79.939			
	49.294	47.676	17.08		
3.325	81.124	79.934			
	49.214	47.577			
3.471	81.160				81.157
A $-\frac{1}{2} \rightarrow -\frac{3}{2}$	80.069			80.068	
	49.204				49.195
B $+\frac{5}{2} \rightarrow +\frac{3}{2}$	47.678			47.684	
	15.11	15.81	16.62	15.20	15.26
	16.82	17.36		17.06	17.06
3.563	81.256			81.30	
B $-\frac{1}{2} \rightarrow -\frac{3}{2}$	79.930				79.929
	47.564			47.68	47.55
	16.78	17.17		17.07	17.06
3.634	81.309			81.306	
	79.898			80.05	79.92
A $+\frac{5}{2} \rightarrow +\frac{3}{2}$	49.324			49.34	49.20
	47.687			47.677	
	15.51	16.45		15.21	15.25

Table 5.3 ENDOR frequencies for RbAl alum. H near cubic field axes.

EPR FIELD 10^{-1} T	ENDOR FREQUENCY MHz OBSERVED		CALCULATED A	B	C	D
2.971	81.139		81.17	81.139	81.16	81.20
	80.021		80.04	80.01	80.04	80.08
A $-\frac{1}{2} \rightarrow -\frac{3}{2}$	49.440	49.177	49.16	49.27	49.46	49.45
	47.801	47.534	47.537	47.63	47.85	47.85
3.023	81.155		81.17	81.15	81.17	81.20
	80.024		80.04	80.00	80.03	80.07
	49.438	49.168	49.160	49.26	49.45	49.445
	47.835	47.572	47.54	47.63	47.835	47.839
3.078	81.167		81.18	81.15	81.175	81.21
	80.033		80.033	80.00	80.033	80.07
	47.580	47.827	47.54	47.62	47.824	47.828
3.135	81.186		81.184	81.16	81.181	81.22
	80.014		80.03	80.00	80.03	80.07
	47.840	47.621	47.54	47.620	47.81	47.82
3.335	81.181		81.21	81.180	81.20	81.24
	80.000		80.02	79.98	80.01	80.05
	49.411	49.176	49.17	49.25	49.407	49.406
$+\frac{1}{2} \rightarrow -\frac{1}{2}$	47.541	47.512	47.53	47.61	47.78	47.78
	14.19	14.67				
	15.04	15.20	15.27	15.60	15.67	15.32
	15.41	15.59	17.16	17.50	17.58	17.21
	15.97	17.95				
3.498	81.199		81.23	81.198	81.22	81.26
	80.010		80.00	79.97	80.00	80.04
	49.394	49.165	49.171	49.25	49.391	49.394
3.548	81.222		81.23	81.20	81.228	81.26
	79.989		80.00	79.97	79.994	80.03
	49.392	49.208	49.17	49.25	49.387	49.390
3.606	81.235		81.238	81.21	81.235	81.27
	79.984		79.99	79.96	79.989	80.03
	49.391	49.215	49.18	49.24	49.383	49.387
3.661	81.228	81.214	81.24	81.217	81.24	81.28
A $+\frac{3}{2} \rightarrow +\frac{1}{2}$	79.964		79.99	79.956	79.98	80.02
	49.184		49.178	49.24	49.38	49.38

Polar coordinates of H with ⟨100⟩ axes (1,10.5,-47)

ANGLES FOR DIFFERENT SITES

SITE	A	B	C	D
THETA θ	55.8	65.2	55.0	44.2
PHI φ	12.7	-0.4	-12.8	0.5
ALPHA α	9.5	-9.5	9.5	-9.5

5.4 ENDOR of RbGa Alum

Typical ENDOR spectra for RbGa alum are shown in Fig. 5.5 for $\vec{H}$ along the [111] direction and in Fig. 5.6 for $\vec{H}$ near the ζ_A axis. The lines along the [111] direction were weak in intensity compared to those along the cubic axes. Very few $\upsilon(\pm 3/2)$ frequencies were measured, but a few strong isolated $\upsilon(\pm 1/2)$ lines were measured and used in the fitting process. To which site, A or BCD, the $\upsilon(\pm 1/2)$ lines on the [111] axis belonged was determined by trial and error. The cubic field axis spectrum was good. The 4 $\upsilon(\pm 3/2)$ lines for each different site were often resolved, as shown in Fig. 5.6. The $\upsilon(\pm 1/2)$ lines were not fitted since too many frequencies appeared in that range of the spectrum.

5.5 Parameters for RbGa Alum

Since the lines at $\upsilon(M)$ and $\upsilon(-M)$ frequencies were not always observed, perturbation theory could not be used to calculate the starting parameters. The $\upsilon_A(\pm 5/2)$ and $\upsilon_A(-1/2)$ frequencies, however,

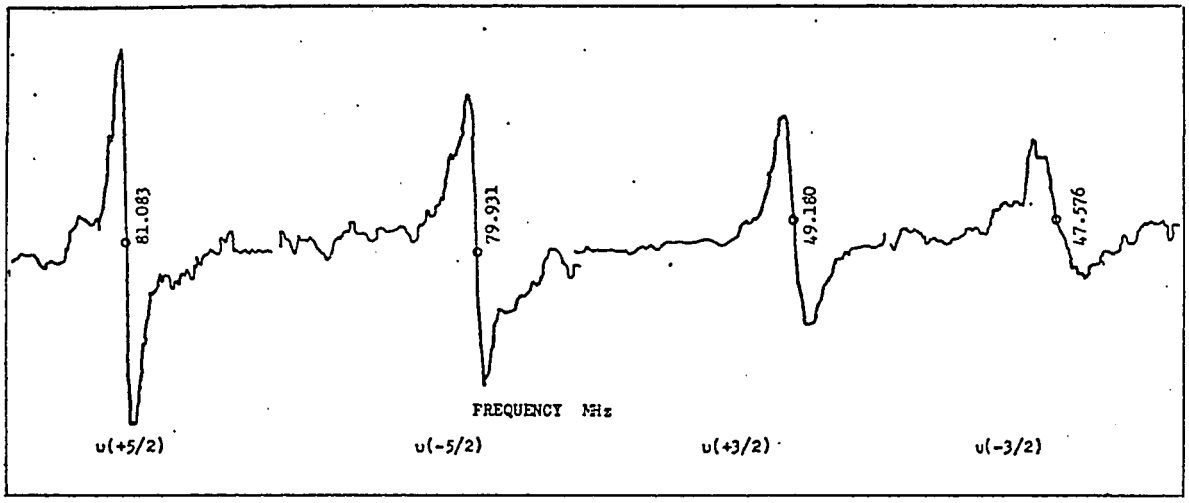

RbGa ALUM H ON [111] AXIS, FIXED ON EPR LINE B $+\frac{3}{2} \rightarrow +\frac{1}{2}$. H = 0.3045 TESLA

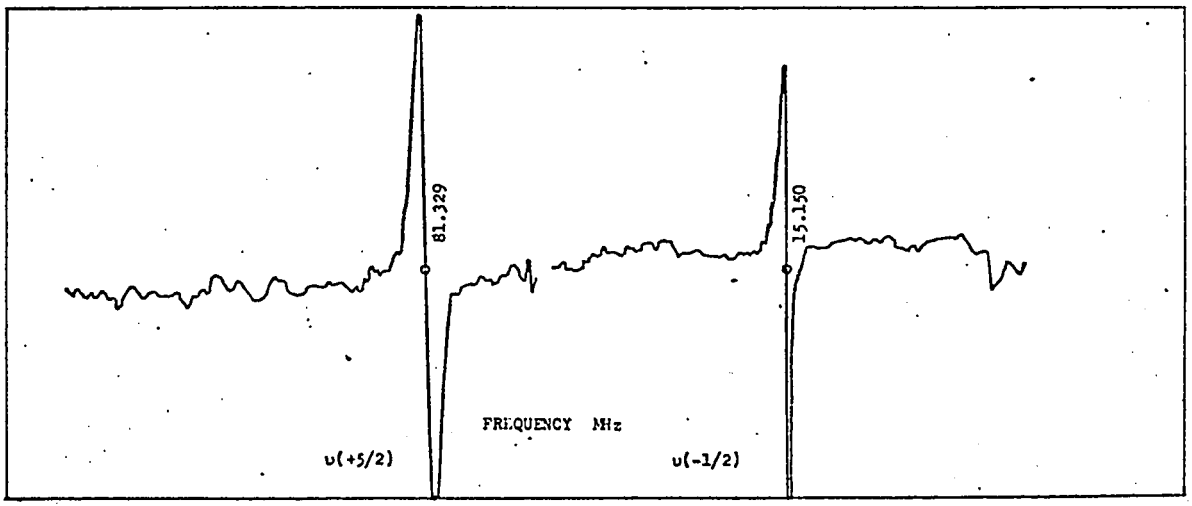

RbGa ALUM H ON [111] AXIS, FIXED ON EPR LINE A $+\frac{5}{2} \rightarrow +\frac{3}{2}$. H = 0.3870 TESLA

Fig. 5.5 ENDOR spectra for RbGa alum.

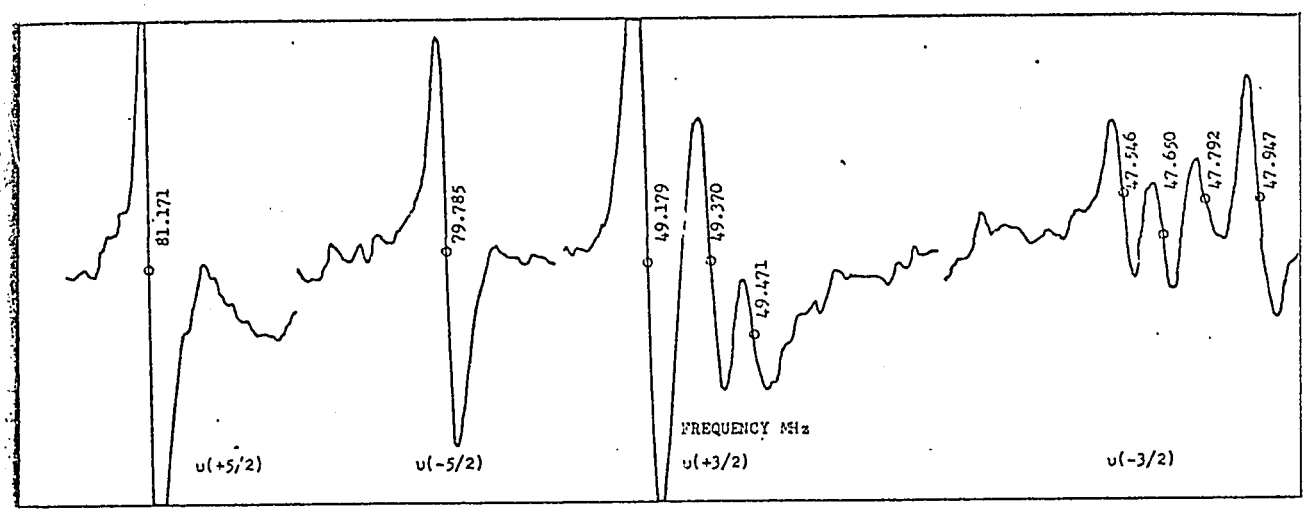

RbGa ALUM H NEAR CUBIC FIELD AXES, FIXED ON EPR LINE $+\frac{1}{2} \rightarrow -\frac{1}{2}$. H = 0.3337 TESLA

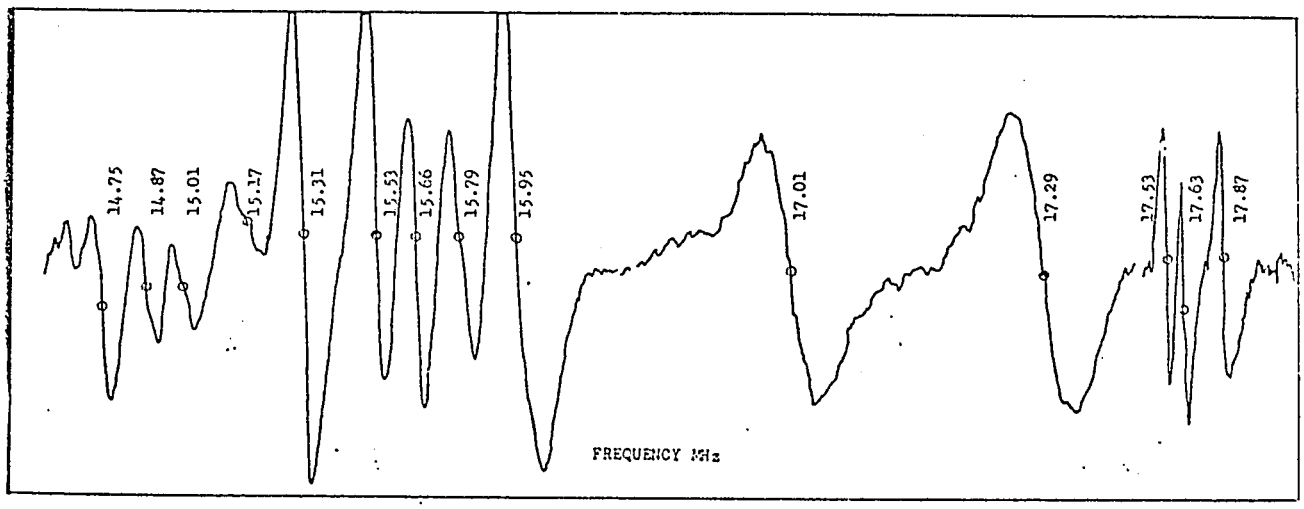

RbGa ALUM H NEAR CUBIC FIELD AXES, FIXED ON EPR LINE $+\frac{1}{2} \rightarrow -\frac{1}{2}$. H = 0.3337 TESLA

Fig. 5.6 ENDOR spectra for RbGa alum.

were easily fitted by iterations on A' $U_{\parallel}$ and g_I. These were close to the values obtained for RbAl alum. Then by iterations of B', $U_{\perp}$, g_I and the angle of rotation about the trigonal axis α, site B of the [111] axis and the cubic axis spectra were fitted. No misalignment error was necessary for the cubic field axes fit. The orientation of $\vec{H}$ near the cubic field was (1,9.5,-45). The observed and calculated frequencies are plotted in Figs. 5.7. and 5.8, and tabulated in Tables 5.4 and 5.5.

The spin Hamiltonian parameters for the ENDOR of $^{57}Fe^{3+}$ in $RbGa(SO_4)_2 \cdot 12H_2O$ are

$g = 2.003$	$g_I = 0.180$
$a/h = 392$ MHz	$A'/h = -32.250$ MHz
$D/h = -252$ MHz	$B'/h = -32.250$ MHz
$F/h = 11$ MHz	$U_{\parallel}/h = 0.007$ MHz
$\alpha = 9.5$ degrees	$U_{\perp}/h = -0.005$ MHz .

From these, the values of A and B are

$A/h = -32.274$ MHz

$B/h = -32.233$ MHz .

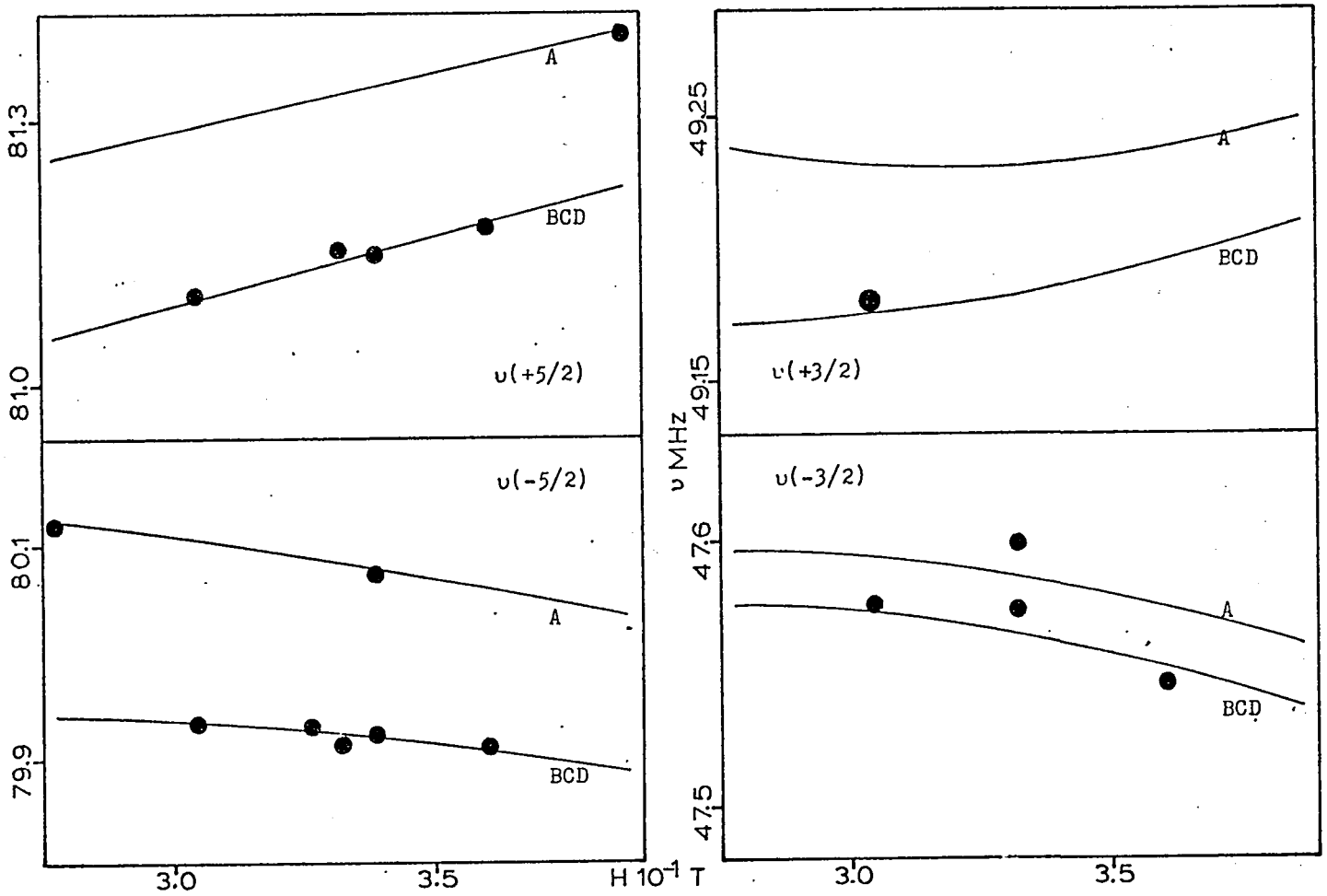

Fig. 5.7 ENDOR frequencies υ vs. the magnetic field $\vec{H}$, for RbGa alum, with $\vec{H}$ along the [111] direction.

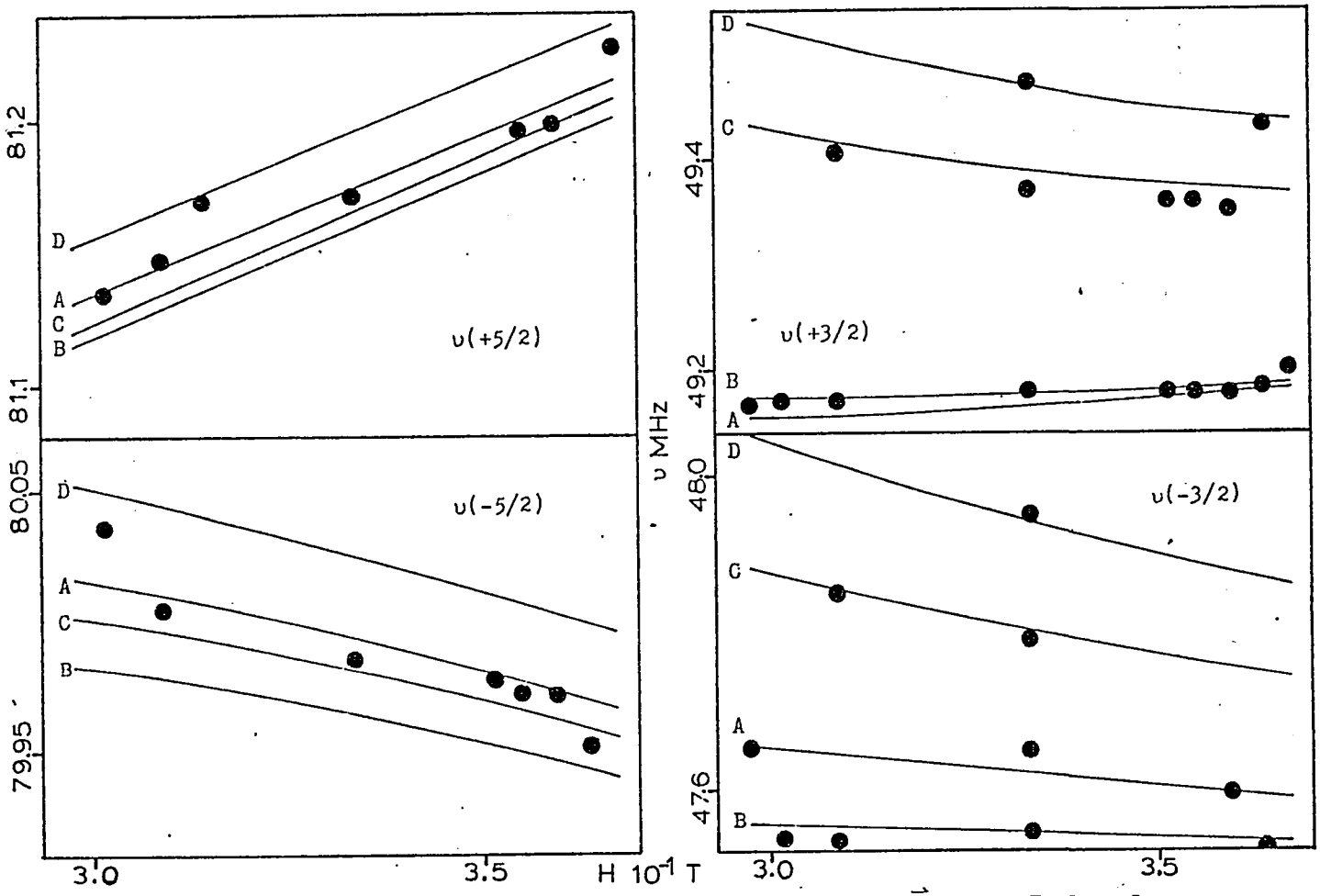

Fig. 5.8 ENDOR frequencies υ vs. the magnetic field $\vec{H}$, for RbGa alum, with $\vec{H}$ near the ζ_A axis.

Table 5.4 ENDOR frequencies for RbGa alum. H on [111] axis.

EPR FIELD 10^{-1} T	ENDOR FREQUENCY MHz OBSERVED			CALCULATED A	CALCULATED BCD
2.776 A $-\frac{3}{2}\rightarrow-\frac{5}{2}$		15.764	80.117 15.649	80.122 15.11	15.648
B $+\frac{3}{2}\rightarrow+\frac{1}{2}$ 3.045			81.083 79.931 49.180 47.576		81.080 79.935 49.175 47.573
3.053 3.068 3.075	81.082 81.086 81.086	49.183 49.185 49.176			
3.267 A $+\frac{3}{2}\rightarrow+\frac{1}{2}$ B $-\frac{5}{2}\rightarrow-\frac{3}{2}$			79.929		79.926
$+\frac{1}{2}\rightarrow-\frac{1}{2}$ 3.323			81.105 79.912 47.574	47.587	81.117 79.923 47.565
3.317	81.112	47.599			
3.390 A $-\frac{3}{2}\rightarrow-\frac{1}{2}$ B $+\frac{5}{2}\rightarrow+\frac{3}{2}$	15.91	79.923 16.02 16.76	81.123 80.073 16.67 17.18	80.077 15.15 17.01	81.125 79.919 15.49 17.15
B $-\frac{3}{2}\rightarrow-\frac{1}{2}$ 3.605			81.148 79.911 47.546		81.153 79.905 47.552
3.589	79.913	47.541			
3.870 A $+\frac{5}{2}\rightarrow+\frac{3}{2}$			81.329 15.150	81.333 15.152	

Table 5.5 ENDOR frequencies for

RbGa alum. Polar coordinates of H with ⟨100⟩ axes (1,9.5,-45)

EPR FIELD 10^{-1} T	ENDOR FREQUENCY MHz OBSERVED			CALCULATED A	B	C	D
2.977			49.168 47.650	49.156 47.656	49.173		
3.018			81.134 80.035 49.170	81.136	49.173		80.049
		47.535	48.07		47.556		48.04
3.092			81.147 80.004	81.145 80.010		79.996	
		49.170	49.405		49.173	49.414	
		47.531	49.851		47.556	47.857	
	14.40	14.51	14.80				
	15.93	16.86	17.14				
3.143			81.169				81.167
$+\frac{1}{2} \rightarrow -\frac{1}{2}$ 3.322	81.175	79.995					
	49.464	49.389					
	49.183	47.947					
3.337			81.171	81.175		81.165	
			79.985	79.993		79.981	
			49.370		49.176	49.388	49.470
	49.471	49.179	47.792	47.62	47.546	47.806	47.940
	47.546	47.650		15.54			
	47.947			17.50	17.88	17.94	17.30
3.352	12.78	13.07	14.80				
	14.95	15.58	15.70				
	15.86	15.99	16.61				
	17.95	17.73	17.07				
3.515			79.977	79.979		79.968	
		49.178	49.360	49.177		49.375	
3.549			81.195	81.201	81.85	81.191	
			79.972	79.977		79.965	
		49.178	49.360	49.178	49.183	49.373	
	13.46	13.32	13.73				
	14.50	15.27	15.50	15.50			15.32
	15.73	15.87	16.07		15.90	15.88	
	16.27						
3.594			81.198	81.206	81.190	81.197	
			79.971	79.973		79.962	
		49.178	49.350	49.181	49.185	49.370	
			47.599	47.595			
3.638			79.952		79.942	79.958	
		49.182	49.432	49.183	49.187		49.441
			47.526		47.526		
3.671			81.227	81.215			81.235
		49.203	49.439	49.185	49.188		49.439
$A\ +\frac{3}{2} \rightarrow +\frac{1}{2}$	15.04	14.67	16.62				
	16.98	17.42	17.16				
			17.37				

ANGLES IN SPIN HAMILTONIAN FOR DIFFERENT SITES		A	B	C	D
SITE					
THETA	θ	55.2	63.7	55.2	45.4
PHI	φ	11.0	0.0	-11.0	0.0
ALPHA	α	9.5	-9.5	9.5	-9.5

5.6 Error of the Hyperfine Parameters

Since the $\upsilon(M)$ lines were fitted within $\pm$ 0.01 MHz, the error on the parameters that produced a 0.01 MHz difference from the best fit values is

$$\Delta A' = \Delta B' = \pm 0.005 \text{ MHz},$$

$$\Delta U_{\parallel} = \Delta U_{\perp} = \pm 0.001 \text{ MHz}.$$

Thus the error on A and B is

$$\Delta A = \Delta B = \pm 0.008 \text{ MHz}.$$

Since

$$g_I = \frac{h}{2H\beta_N} [\, \upsilon(M) - \upsilon(-M) \,]$$

and $\Delta\upsilon(\pm M) = \pm 0.01$ MHz

then $\Delta g_I = \pm 0.004$.

The eigenvalues of the Hamiltonian matrix for sites B,C, and D in the [111] direction and on the cubic field axes were found to be very sensitive to the angle of rotation about the trigonal axis, α. Thus α could be determined within $\pm$ 0.5 degrees.

CHAPTER 6

DISCUSSION OF THE RESULTS

6.1 Fine Structure Parameters

The fine structure parameters found for RbAl alum at a temperature of 4.2 K are nearly the same as those found by Bleaney and Trenam [2] at a temperature of 20 K, as shown in Table 6.1. The sign of the cubic field splitting parameter a is positive, as determined experimentally by Geschwind for RbAl alum [16]. Theoretically, Watanabe [17] showed that the sign of a should always be positive in any cubic environment. The cubic field splitting parameter a in the alums has nearly the same constant value, as showed by Bleaney and Trenam [2]. The values obtained in the present work for RbAl and RbGa alums are exactly the same.

The axial crystal field parameter D can vary greatly, and be positive or negative, depending on the type of alum considered [2]. The magnitude of D is related to the strength of the trigonal distortion.

Table 6.1 Fine structure parameters for Fe^{3+} in some alums

Exp. results	Temperature K	Splitting parameter 10^{-4} cm^{-1} a	D	F	g
$RbAl(SO_4)_2 \cdot 12H_2O$	4.2	133(4)	-31(2)	4(2)	2.003(3)
$RbGa(SO_4)_2 \cdot 12H_2O$	4.2	133(4)	-84(2)	4(2)	2.003(3)
Bleaney's and Trenam's results:					
$RbAl(SO_4)_2 \cdot 12H_2O$	20	134(1)	-31(2)	3(1)	2.003(1)
$KAl(SeO_4)_2 \cdot 12H_2O$	20	127(2)	115(1)	2(1)	2.003(1)

The number in parenthesis is the error on the last digit.

Hence RbGa alum is more trigonally distorted than is RbAl alum. The relative amount of distortion may be due to the larger size of the trivalent Ga ion compared to the smaller Al ion. It is uncertain in the case of the Fe^{3+} impurity ion whether the negative sign of D represents a trigonal extension or compression of the octahedron.

The spectroscopic splitting parameter g was found to be isotropic within experimental error. The obtained value of g = 2.003 is close to the free spin value of 2.0023, as expected for S-state ions.

6.2 Angle of Rotation α of the Cubic Field Axes About the Trigonal Axis

The angle α was found by EPR and ENDOR measurements to be 9.5 ± 0.5 degrees. This is in accord with the value of 9.3 ± 0.5 degrees found by Bleaney and Trenam [2]. The angle of rotation of the cubic field axes should be the same as the angle of rotation of the octahedron of water molecules about the trigonal axis. If (v, $\bar{v}$, u) is the position of a water molecule in the crystal, then as shown in

appendix 2,

$$\cos\alpha = [\ 1 + (v/u)^2\ ]^{-\frac{1}{2}}.$$

From X-ray analysis of RbAl alum, Larson and Cromer [18] found that $v/u = 0.13$ and $\alpha = 13$ degrees. From neutron diffraction work, Bacon and Gardner [8] found the angle α to be about 9.0 ± 1.0 degrees. Hence the rotation of the cubic field axes is related to the rotation of the octahedron of water molecules about the trigonal axis.

6.3 Hyperfine Structure Parameters

It was not known beforehand if the spin Hamiltonian concept could be applied successfully to describe the hyperfine levels in alums. The only previous ENDOR work on $^{57}Fe^{3+}$ was for cubic symmetry with the Fe^{3+} ion coordinated to O_2^- ions in MgO [11]. No work had been done on ENDOR in a hydrated complex. The hyperfine structure parameters could not be measured by EPR methods since the hyperfine splittings were masked by the large EPR line broadening, which is typical of hydrated complexes. The only successful attempt was made by

Culvahouse and Olsen [19] in the EPR of $^{57}Fe^{3+}$ in double nitrate crystals. They only reported the hyperfine parameter

$$A' = 32.7 \pm 1 \text{ MHz}.$$

The value of the hyperfine parameters measured in the present work using the ENDOR technique are improved by two significant figures over ordinary EPR methods.

In Fig. 3.6, showing the EPR spectrum of RbGa alum for $\vec{H}$ along the [111] axis, the EPR lines BCD $\pm 1/2 \leftrightarrow \pm 3/2$ are split into a doublet. The average separation between the doublets is 45 MHz. It is not known whether the splitting is due to misalignment of the magnetic field or hyperfine splitting, because a misalignment of 1 degree would also split the EPR line. Since a misalignment of 1 degree would also split the $\upsilon_{BCD}(\pm 3/2)$ ENDOR lines, and since these lines were not clearly observed (Fig. 5.7), then one cannot tell if the field was misaligned or not.

The spin Hamiltonian developed in chapter

4 for trigonal symmetry permitted an adequate description of the ENDOR spectrum of $^{57}Fe^{3+}$ in the RbAl and RbGa alums. Hence the substitution of the paramagnetic ion in the host alum crystals did not appreciably alter the symmetry at the ion site as sometimes happens [20]. Hyperfine structure parameters of $^{57}Fe^{3+}$ for various crystals are listed in Table 6.2. For the alums, A and B are chosen as the parameters for the $\vec{S}\cdot\vec{I}$ term instead of A' and B' . This is consistent with previous work [11] and with symmetry considerations of group theory.

The anisotropy of the hyperfine parameters due to the trigonal distortion is minimal. The difference A-B is about 0.07 MHz for RbAl alum and 0.04 MHz for RbGa alum. Within experimental error, the B coefficients for RbAl and RbGa alum are equal, showing consistency in the results. The A term are also nearly equal. Thus a trigonal distortion does not affect the SI terms. As in the case of the B parameters, the $U_\perp$ for RbAl and RbGa alums have the same value within experi-

Table 6.2 Hyperfine structure parameters of $^{57}Fe^{3+}$ for various crystals

Crystal	Hyperfine parameters MHz A	B	$U_{\parallel}$	$U_{\perp}$	g_I
MgO [11]	-30.176(2)	-30.176(2)	-0.0057(3)	-0.0057(3)	0.1805(1)
$RbAl(SO_4)_2 \cdot 12H_2O$	-32.30(1)	-32.23(1)	-0.021(1)	-0.004(1)	0.180(4)
$RbGa(SO_4)_2 \cdot 12H_2O$	-32.27(1)	-32.23(1)	0.007(1)	-0.005(1)	0.180(4)

The number in parenthesis is the error on the last digit.

mental error. However U_{II} differs greatly for the two alums. Hence the S^3I term along a trigonal axis is affected by a trigonal distortion.

The value of the nuclear spectroscopic splitting parameter $g_I = 0.180 \pm 0.004$ is in accord with the value of 0.1805 ± 0.0001 found by Locher and Geschwind [11]. Less accuracy is obtained in the present case since the Fe^{3+} ion exists in a hydrated environment, which causes broadening of the ENDOR lines. Also the presence of 4 sites in the crystal reduces the resolution of the ENDOR lines when $\vec{H}$ is along the [111] direction.

The signs of the hyperfine parameters are in accord with the work of Locher and Geschwind [11] in MgO. Also the signs give a correct interpretation of the identification of the ENDOR lines given in Tables 5.2 and 5.4. When $\vec{H}$ is along a [111] direction and set on the EPR line $X(M \rightarrow M-1)$ with $X=A,B$, the ENDOR frequencies $\upsilon_X(M)$ and $\upsilon_X(M-1)$ should be observed since they are the most probable. An examination of Tables 5.2 and 5.4 shows this to be

the case for most EPR lines. On the cubic field axis direction the occurence of 4 sites somewhat masks this effect.

For the case of trigonal symmetry, measurements are usually taken along the z axis and in a direction perpendicular to it. Measurements along a ⟨110⟩ direction should directly yield values of B and $U_{\perp}$, since the first order contribution to A, $U_{\parallel}$, $U_{\perp}'$, and $U_{\parallel}'$ goes to zero. But in that direction the EPR field separations are at minima, and misalignment of the magnetic field becomes critical, causing large errors in the ENDOR eigenvalues for the two nonequivalent sites (AC) and (BD). On the other hand, for measurements along the [111] axis and near the cubic field axis ζ_A, misorientation of the magnetic field is minimal for site A.

In conclusion it can be said that the measurement of the EPR fine structure and ENDOR hyperfine structure parameters of $^{57}Fe^{3+}$ in RbAl and RbGa alums gives values that are in accord with those obtained by others in systems where similar types of measurements were made. It

would be worthwhile to extend these measurements to other types of alums and hydrated crystals in order to classify crystal behaviour from the point of view of parameter magnitudes and signs. In this way one can obtain a better understanding of the physical behaviour of the $^{57}Fe^{3+}$ S-state ion in hydrated crystals, and also evaluate the available theory.

APPENDIX 1

Directions of the Cubic Field Axes

The directions of the $\xi\eta\zeta$ axes rotated from the $\langle 001 \rangle$ axes are given, for each site, by

$$R^{-1} R_\alpha^{-1} R \langle 001 \rangle .$$

Here R is the direction cosine matrix of the trigonal set of axes with respect to the $\langle 001 \rangle$ axes for each site. The axis of abscissa in the trigonal plane of each site is chosen as the projection of the [001] axis in that plane. Thus the four R matrices are

$$R_A = \begin{bmatrix} -1/\sqrt{6} & -1/\sqrt{6} & 2/\sqrt{6} \\ 1/\sqrt{2} & -1/\sqrt{2} & 0 \\ 1/\sqrt{3} & 1/\sqrt{3} & 1/\sqrt{3} \end{bmatrix}, \quad R_B = \begin{bmatrix} 1/\sqrt{6} & -1/\sqrt{6} & 2/\sqrt{6} \\ 1/\sqrt{2} & 1/\sqrt{2} & 0 \\ -1/\sqrt{3} & -1/\sqrt{3} & 1/\sqrt{3} \end{bmatrix},$$

$$R_C = \Pi R_A \Pi \quad , \quad R_D = \Pi R_B \Pi \quad ,$$

where $$\Pi = \begin{bmatrix} -1 & 0 & 0 \\ 0 & -1 & 0 \\ 0 & 0 & -1 \end{bmatrix}$$

by properties of the $\frac{2}{m}3$ point group. R_α is the rotation matrix about the trigonal axis, and is given by

$$R_\alpha = \begin{bmatrix} \cos\alpha & \sin\alpha & 0 \\ -\sin\alpha & \cos\alpha & 0 \\ 0 & 0 & 1 \end{bmatrix} .$$

For sites A and C, α is positive, while for sites B and D it is negative. This is due to the choice of trigonal axes. For example, the direction of the ζ axis for site A will be $[efd] = R_A^{-1} R_\alpha^{-1} R_A [001]$.

The positions of the $\xi\eta\zeta$ axes are determined primarily by the rotation of the octahedra of water about the trigonal axes. For the rotation about the [111] axis, we let the coordinates of the water molecule at (v,-v,u) with respect to the trigonal axes of site A be

$$R_A(v,-v,u) = (x,y,z).$$

A trigonal distortion only affects the z component. The angle of rotation α will thus be the angle between the projection of (x,y,z) in the trigonal plane, (x,y), and the projection of the [001] axis in the same plane, (1,0). Hence

$$\cos\alpha = \frac{x}{\sqrt{x^2 + y^2}} = \frac{u}{\sqrt{u^2 + 3v^2}} .$$

Similar equations for the position of the $\xi\eta\zeta$ axes were stated by Bleaney & Trenam [2].

APPENDIX 2

Numerical Rotation of the S^3I Term from the Cubic Axes to the Trigonal Axes

In the program below the S^3I term on the cubic field axes is written as

$$SX^3IX + SY^3IY + SZ^3IZ - 101/20\ \vec{S}\cdot\vec{I} \quad .$$

To rotate this term to the trigonal axes the SX, SY, SZ, vector operators are transformed according to the relation

$$\begin{pmatrix} SX \\ SY \\ SZ \end{pmatrix} = \begin{bmatrix} 1/\sqrt{6} & -1/\sqrt{2} & 1/\sqrt{3} \\ -1/\sqrt{6} & -1/\sqrt{2} & 1/\sqrt{3} \\ 2/\sqrt{6} & 0 & 1/\sqrt{3} \end{bmatrix} \begin{pmatrix} SXD \\ SYD \\ SZD \end{pmatrix} .$$

(Transposed Rotation Matrix A**(-1))

SXD, SYD and SZD are the vector operators whose axis of quantization is the trigonal axis. Thus

$$SZD = \begin{bmatrix} 2.5 & & & & & \\ & 1.5 & & & & \\ & & 0.5 & & & \\ & & & -0.5 & & \\ & & & & -1.5 & \\ & & & & & -2.5 \end{bmatrix}$$

and SXD and SYD have the usual matrix form. In the program below, the transposed rotation matrix A**(-1) is expressed in terms of the Euler's angle from the cubic to the trigonal system.

Similarly to SX,SY,SZ, the nuclear vectors IX,IY, and IZ are expressed in terms of IXD,IYD,IZD, where

$$IZD = \begin{bmatrix} \frac{1}{2} & 0 \\ 0 & -\frac{1}{2} \end{bmatrix}, \quad IXD = \begin{bmatrix} 0 & \frac{1}{2} \\ \frac{1}{2} & 0 \end{bmatrix}, \quad IYD = \begin{bmatrix} 0 & (0,-\frac{1}{2}) \\ (0,\ \frac{1}{2}) & 0 \end{bmatrix} .$$

Complex numbers are written as

(real part, imaginary part)

For the S^3I term rotated to the trigonal axes, only the real part of the matrix elements are given since the imaginary parts are all zero.

```
C       APPENDIX 2
C       RO TATION OF SPIN HAMILTONIAN TERMS WITH EULER'S ANGLES
        REAL D(12,12)
        COMPLEX U(12,12),S(12,12)
        COMPLEX SXD(6,6),SYD(6,6),SZD(6,6),SX(6,6),SY(6,6),SZ(6,6)
        COMPLEX IX(2,2),IY(2,2),IZ(2,2),IXD(2,2),IYD(2,2),IZD(2,2)
C        SPIN MATRICES
        READ(5,1) SXD
        READ(5,1) SYD
        READ(5,1) SZD
1       FORMAT(6F10.6)
        READ(5,20) IXD
        READ(5,20) IYD
        READ(5,20) IZD
20      FORMAT(8F5.1)
C       TH,PH,PS  THETA,PHI, PSI,  EULER'S ANGLES
        READ(5,9) THD,PHD,PSD
9       FORMAT(3E20.7)
        DTR=0.1745329E-1
        TH=THD*DTR
        PH=PHD*DTR
        PS=PSD*DTR
        WRITE(6,12) THD,PHD,PSD
12      FORMAT('1','EULER S ANGLES',T25,'THETA =',F10.5/T25,'PHI   =',
       1F10.5/T25,'PSI   =',F10.5)
C       ELEMENTS OF TRANSPOSED ROTATED MATRIX, A**(-1),. REF. GOLDSTEI"
C       'CLASSICAL MECHANICS'.
        CTH=COS(TH)
        STH=SIN(TH)
        CPH=COS(PH)
        SPH=SIN(PH)
        CPS=COS(PS)
        SPS=SIN(PS)
        A11= CPS*CPH  -CTH*SPH*SPS
        A12=-SPS*CPH  -CTH*SPH*CPS
        A13= STH*SPH
        A21= CPS*SPH  +CTH*CPH*SPS
        A22=-SPS*SPH  +CTH*CPH*CPS
        A23=-STH*CPH
        A31= STH*SPS
        A32=STH*CPS
        A33= CTH
        WRITE(6,5) A11,A12,A13,A21,A22,A23,A31,A32,A33
5       FORMAT('-','TRANSPOSED ROTATION MATRIX A**(-1)'/('0',3F20.5))
C       TRANSFORMATION FOR SX,SY,SZ
        DO4 I=1,6
        DO4 J=1,6
        SX(I,J)= A11*SXD(I,J)  +A12*SYD(I,J)  +A13*SZD(I,J)
        SY(I,J)= A21*SXD(I,J)  +A22*SYD(I,J)  +A23*SZD(I,J)
        SZ(I,J)= A31*SXD(I,J)  +A32*SYD(I,J)  +A33*SZD(I,J)
4       CONTINUE
        WRITE(6,6)  ((SX(I,J),J=1,6),I=1,6)
        WRITE(6,7)  ((SY(I,J),J=1,6),I=1,6)
        WRITE(6,8)  ((SZ(I,J),J=1,6),I=1,6)
6       FORMAT('-','ROTATED COMPLEX SPIN MATRICES'//
       1       '-','SX'/(' ',6('(',F8.5,',',F8.5,') ')))
7       FORMAT('-','SY'/(' ',6('(',F8.5,',',F8.5,') ')))
8       FORMAT('-','SZ'/(' ',6('(',F8.5,',',F8.5,') ')))
```

```
C       TRANSFORMATION FOR IX,IY,IZ
        DO 21 I=1,2
        DO 21 J=1,2
        IX(I,J)= A11*IXD(I,J) +A12*IYD(I,J) +A13*IZD(I,J)
        IY(I,J)= A21*IXD(I,J) +A22*IYD(I,J) +A23*IZD(I,J)
        IZ(I,J)= A31*IXD(I,J) +A32*IYD(I,J) +A33*IZD(I,J)
21      CONTINUE
        WRITE(6,23)  ((IX(I,J),J=1,2),I=1,2)
        WRITE(6,24)  ((IY(I,J),J=1,2),I=1,2)
        WRITE(6,25)  ((IZ(I,J),J=1,2),I=1,2)
23      FORMAT('-','IX'/(' ',2('(',F8.5,',',F8.5,')')))
24      FORMAT('-','IY'/(' ',2('(',F8.5,',',F8.5,')')))
25      FORMAT('-','IZ'/(' ',2('(',F8.5,',',F8.5,')')))
C                  SZ*SZ*SZ*IZ+SY*SY*SY*IY+SX*SX*SX*IX-101/20*S*I
        DO 30 I=1,6
        DO 30 J=1,6
        SZD(I,J)=0.0E0
        SYD(I,J)=0.0E0
        SXD(I,J)=0.0E0
        DO 30 K=1,6
        DO 30 L=1,6
        SZD(I,J)=SZD(I,J)  + SZ(I,K)*SZ(K,L)*SZ(L,J)
        SYD(I,J)=SYD(I,J)  + SY(I,K)*SY(K,L)*SY(L,J)
        SXD(I,J)=SXD(I,J)  + SX(I,K)*SX(K,L)*SX(L,J)
30      CONTINUE
        DO 31 I=1,6
        DO 31 J=1,6
        DO 31 K=1,2
        DO 31 L=1,2
        U(2*(I-1)+K,2*(J-1)+L) = SZD(I,J)*IZ(K,L) + SYD(I,J)*IY(K,L) +
       1 SXD(I,J)*IX(K,L)
        S(2*(I-1)+K,2*(J-1)+L) = SZ(I,J)*IZ(K,L) + SY(I,J)*IY(K,L) +
       1 SX(I,J)*IX(K,L)
31      CONTINUE
        DO 33 I=1,12
        DO 33 J=1,12
        D(I,J)=REAL(U(I,J) - 101./20.*S(I,J))
        IF(ABS(D(I,J)).LT.1.E-3) D(I,J)=0.0E0
33      CONTINUE
        WRITE(6,34)  ((D(I,J),J=1,12),I=1,12)
34      FORMAT('1'////'-',5X,'SZ*SZ*SZ*IZ + SY*SY*SY*IY + SX*SX*SX*IX -
       21/20*S*I  ROTATED TO THE TRIGONAL AXES'///('0',12F10.4))
        STOP
        END
```

EULER S ANGLES THETA = 54.73560
PHI = 135.00000
PSI = 90.00000

TRANSPOSED ROTATION MATRIX A**(-1)

-0.40825	0.70711	0.57735
-0.40825	-0.70711	0.57735
0.81650	0.00000	0.57735

ROTATED COMPLEX SPIN MATRICES

SX

(1.44338, 0.0)	(-0.45644,-0.79057)	(0.0 , 0.0)	(0.0 , 0.0)	(0.0 , 0.0)	(0.0 , 0.0)	(0.0 , 0.0)	(0.0 , 0.0)
(-0.45644, 0.79057)	(0.86603, 0.0)	(-0.57735,-1.00000)	(0.0 , 0.0)	(0.0 , 0.0)	(0.0 , 0.0)	(0.0 , 0.0)	(0.0 , 0.0)
(0.0 , 0.0)	(-0.57735, 1.00000)	(0.28868, 0.0)	(-0.61237,-1.06066)	(0.0 , 0.0)	(-0.61237,-1.06066)	(0.0 , 0.0)	(0.0 , 0.0)
(0.0 , 0.0)	(0.0 , 0.0)	(-0.61237, 1.06066)	(0.0 , 0.0)	(-0.28868, 0.0)	(-0.57735,-1.00000)	(0.0 , 0.0)	(0.0 , 0.0)
(0.0 , 0.0)	(0.0 , 0.0)	(0.0 , 0.0)	(-0.57735, 1.00000)	(-0.57735, 1.00000)	(-0.86603, 0.0)	(-0.45644,-0.79057)	
(0.0 , 0.0)	(0.0 , 0.0)	(0.0 , 0.0)	(0.0 , 0.0)	(0.0 , 0.0)	(-0.45644, 0.79057)	(-1.44339, 0.0)	

SY

(1.44337, 0.0)	(-0.45643, 0.79057)	(0.0 , 0.0)	(0.0 , 0.0)	(0.0 , 0.0)	(0.0 , 0.0)	(0.0 , 0.0)	(0.0 , 0.0)
(-0.45643,-0.79057)	(0.86602, 0.0)	(-0.57735, 1.00000)	(0.0 , 0.0)	(0.0 , 0.0)	(0.0 , 0.0)	(0.0 , 0.0)	(0.0 , 0.0)
(0.0 , 0.0)	(-0.57735,-1.00000)	(0.28867, 0.0)	(-0.61237, 1.06066)	(0.0 , 0.0)	(-0.57735, 1.00000)	(0.0 , 0.0)	(0.0 , 0.0)
(0.0 , 0.0)	(0.0 , 0.0)	(-0.61237,-1.06066)	(0.0 , 0.0)	(-0.28867, 0.0)	(-0.57735,-1.00000)	(-0.86602, 0.0)	(-0.45643, 0.79057)
(0.0 , 0.0)	(0.0 , 0.0)	(0.0 , 0.0)	(-0.57735,-1.00000)	(-0.57735,-1.00000)	(-0.45643,-0.79057)	(-1.44337, 0.0)	
(0.0 , 0.0)	(0.0 , 0.0)	(0.0 , 0.0)	(0.0 , 0.0)	(0.0 , 0.0)	(-0.45643,-0.79057)	(-1.44337, 0.0)	

SZ

(1.44338, 0.0)	(0.91287,-0.00000)	(0.0 , 0.0)	(0.0 , 0.0)	(0.0 , 0.0)	(0.0 , 0.0)	(0.0 , 0.0)	(0.0 , 0.0)
(0.91287, 0.00000)	(0.86603, 0.0)	(1.15470,-0.00000)	(0.0 , 0.0)	(0.0 , 0.0)	(0.0 , 0.0)	(0.0 , 0.0)	(0.0 , 0.0)
(0.0 , 0.0)	(1.15470, 0.00000)	(0.28868, 0.0)	(1.22474,-0.00000)	(0.0 , 0.0)	(1.15470,-0.00000)	(0.0 , 0.0)	(0.0 , 0.0)
(0.0 , 0.0)	(0.0 , 0.0)	(1.22474, 0.00000)	(-0.28868, 0.0)	(1.15470, 0.00000)	(-0.86603, 0.0)	(0.91287,-0.00000)	
(0.0 , 0.0)	(0.0 , 0.0)	(0.0 , 0.0)	(1.15470, 0.00000)	(0.0 , 0.0)	(0.91287, 0.00000)	(-1.44339, 0.0)	
(0.0 , 0.0)	(0.0 , 0.0)	(0.0 , 0.0)	(0.0 , 0.0)	(0.0 , 0.0)	(0.91287, 0.00000)	(-1.44339, 0.0)	

IX

(0.28868, 0.0)	(-0.20412,-0.35355)
(-0.20412, 0.35355)	(-0.28868, 0.0)

IY

(0.28867, 0.0)	(-0.20412, 0.35355)
(-0.20412,-0.35355)	(-0.28867, 0.0)

IZ

(0.28868, 0.0)	(0.40825,-0.00000)
(0.40825, 0.00000)	(-0.28868, 0.0)

SZ*SZ*SZ*IZ + SY*SY*SY*IY + SX*SX*SX*IX - 101/20*S*I

-1.0000	0.0	0.0	0.0	0.0	3.3541	1.1180	0.0	0.0	0.0	0.0	0.0
0.0	1.0000	1.3416	0.0	0.0	0.0	0.0	-1.1180	0.0	0.0	0.0	0.0
0.0	1.3416	1.4000	0.0	0.0	0.0	0.0	1.5000	1.4142	0.0	0.0	0.0
0.0	0.0	0.0	-1.4000	-0.4243	0.0	0.0	0.0	0.0	-1.4142	0.0	0.0
0.0	0.0	0.0	-0.4243	0.8000	0.0	0.0	0.0	0.0	-1.5000	1.1180	0.0
3.3541	0.0	0.0	0.0	0.0	-0.8000	-1.2000	0.0	0.0	0.0	0.0	-1.1180
1.1180	0.0	0.0	0.0	0.0	-1.2000	-0.8000	0.0	0.0	0.0	0.0	-3.3541
0.0	-1.1180	1.5000	0.0	0.0	0.0	0.0	0.8000	-0.4243	0.0	0.0	0.0
0.0	0.0	1.4142	0.0	0.0	0.0	0.0	-0.4243	-1.4000	0.0	0.0	0.0
0.0	0.0	0.0	-1.4142	-1.5000	0.0	0.0	0.0	0.0	1.4000	1.3416	0.0
0.0	0.0	0.0	0.0	1.1180	0.0	0.0	0.0	0.0	1.3416	1.0000	0.0
0.0	0.0	0.0	0.0	0.0	-1.1180	-3.3541	0.0	0.0	0.0	0.0	-1.0000

These are the matrix elements of the $[S_\xi^3 + S_\eta^3 + S_\zeta^3 - 101/20\ \vec{S}\cdot\vec{I}]$ term rotated to trigonal axes. These matrix elements are the same as the coefficients for $U_{\parallel}$, $U_{\perp}$, $U'_{\parallel}$ and $U'_{\perp}$ in the spin Hamiltonian matrix elements in table 4.1.

APPENDIX 3

First Order Contribution of S^3I Terms

Under a rotation of angle θ about the y axis, as described in section 4.1, the diagonal terms of some S^3I terms are given below .

$$S_z^3 I_z \longrightarrow [S_z^3 \cos^3\theta + \{S_+ S_z S_-\} \sin^2\theta\cos\theta] I_z \cos\theta$$

where $\{S_+ S_z S_-\}$ represents the six permutations of $S_+ S_z S_-$.

$$S_+^3 I_z \longrightarrow [S_z^3 \sin^3\theta - S_+ S_z S_- \sin^3\theta/4] I_z \cos\theta$$

$$S_+ S_z S_+ I_+ \rightarrow [S_z^3 \sin^2\theta\cos\theta + \tfrac{1}{2}(S_z S_+ S_- + S_- S_+ S_z)\sin^2\theta\sin^2(\theta/2) - \tfrac{1}{2}(S_z S_- S_+ + S_+ S_- S_z)\sin^2\theta\cos^2(\theta/2) - \tfrac{1}{4}(S_+ S_z S_- + S_- S_z S_+)\sin^2\theta\cos\theta] I_z \sin\theta$$

$$S_-^2 S_+ + S_- S_+ S_- + S_+ S_-^2 = 3S_- S_+ S_- - 2S_-$$

$$S_- S_+ S_- I_+ \rightarrow [S_z^3 \sin^3\theta + (S_z S_+ S_- + S_- S_+ S_z)\sin\theta\cos^4(\theta/2) + (S_z S_- S_+ + S_+ S_- S_z)\sin\theta\cos^4(\theta/2) - (S_+ S_z S_- + S_- S_z S_+)\sin^3\theta/4] I_z \sin\theta$$

COMMUTATION RELATIONS

$$S_z S_+ S_- + S_- S_+ S_z = 2S(S+1)S_z - 2S_z^3$$

$$S_z S_- S_+ + S_+ S_- S_z = 2S(S+1)S_z - 2S_z^3$$

$$S_+ S_z S_- + S_- S_z S_+ = 2S(S+1)S_z - 2S_z^3 - 2S_z$$

Thus $\{S_+ S_z S_-\} = 2(3S^2+3S-1)S_z - 6S_z^3$.

APPENDIX 4

Program for the Exact Diagonalization of the Spin Hamiltonaian Matrix

In the program below the parameters

G , GP, AC, D, F, AI, BI, GIZ, GIP, U1, U2, U3, U4,

represent the spin Hamiltonian parameters

$g_{\parallel}$, $g_{\perp}$, a, D, F, A', B', $g_I^{\parallel}$, $g_I^{\perp}$, $U_{\parallel}$, $U_{\parallel}'$, $U_{\perp}$, $U_{\perp}'$,

respectively. The units of the parameters are in MHz, while those of the spin Hamiltonian matrix elements are in GHz. The conversion factors X and Y are

$$X = \beta/h \quad (\mathrm{GHz}/10^{-1}\ \mathrm{T})$$

$$Y = \beta_N/h \quad (\mathrm{GHz}/10^{-1}\ \mathrm{T}).$$

Instead of working with A and B, the program was written in terms of

$$A' = A + \frac{2}{15}(3S^2 + 3S - 1)U_{\parallel}$$

$$B' = B + \frac{2}{15}(3S^2 + 3S - 1)U_{\perp},$$

since the first order perturbation theory gives directly the value of A' and B'.

The subroutine EIGCH employed to diagonalize the spin Hamiltonian matrix was taken from the IMSL library [15], which is incorporated in the computer. Its function is to calculate the eigenvalues of a

complex Hermitian matrix. Only the elements on and below the main diagonal elements are stored. If [A] is a Hermitian matrix whose elements are

$$[A] = \begin{bmatrix} a_{11} & a_{12} & a_{13} & \cdots \\ a_{21} & a_{22} & a_{23} & \cdots \\ a_{31} & a_{32} & a_{33} & \cdots \\ a_{41} & & & \\ \vdots & & & \end{bmatrix}$$

then [A] is reduced to the vector

$$(a_{11}, a_{21}, a_{22}, a_{31}, a_{32}, a_{33}, a_{41} \cdots)$$

and stored as

$$(A(1), A(2), A(3), A(4), A(5), A(6), A(7), \ldots)$$

This subroutine also incorporates a check on how accurate the eigenvalues are. This check was executed and the performance of the subroutine was found to be excellent. Thus the floating point error on the eigenvalues was at a minimum.

```
C     ENDOR FIT WITH IMSL MATRIX DIAGONALIZATION SUBROUTINE EIGCH
      IMPLICIT REAL*8(A-H,O-Z)
      COMPLEX*16 A(78),EPA
      INTEGER N/12/,IJOB/0/,IZ/0/,NC(2)/2,4  /,CP(4)/'A','B','C','D'/
      DIMENSION TH(4),PH(4),ALPHA(4),H(14),U(4),S(12),DEL(6),WK(36),
     1          VI(40,6),TEXT(9),P(40),T(30)
C     N IS THE ORDER OF THE MATRIX
C     IJOB=0  IZ=0  AND WK(36)  ARE TO COMPUTE EIGENVALUES ONLY IN EIG
C     NC IS THE NUMBER OF NON-EQUIVALENT SITES
C     VI CONTAINS THE OBSERVED ENDOR FREQUENCIES
C     S CONTAINS THE EIGENVALUES OR THE ENERGY LEVELS
C     DEL CONTAINS THE CALCULATED ENDOR FREQUENCIES
C     UNITS OF QUANTITIES AT INPUT
C     MAGNETIC FIELD  H  1.0D-1 TESLA
C     AC,D,F,AI,BI,U          MEGAHERTZ
      READ(5,2) G,GP,GIZ,GIP,AC,D,F,AI,BI,U,ALPHA
2     FORMAT(4F10.4,3P3F10.4/6F10.4/0P4F10.4)
      READ(5,6) P,T
6     FORMAT(10A8)
      WRITE(6,8) G,GIZ,AC,D,F,AI,BI,U
C     DR CONVERTS DEGREES TO RADIANS
      DR=0.174532925D-1
C     X AND Y KEEP UNITS IN GIGAHERTZ IN THE HAMILTONIAN MATRIX
      X=1.399611D0
      Y=7.622700D-4
C     UNITS OF X AND Y   GHZ/(1.0D-1 TESLA)
      DO 53 IIK=1,2
      READ(5,101) TEXT,TH,PH
101   FORMAT(9A8/4F10.4/4F10.4)
      READ(5,1) NH,(H(I),I=1,NH)
1     FORMAT(I5/(6F10.4))
      READ(5,1) NV,((VI(I,J),J=1,6),I=1,NV)
      WRITE(6,T) TEXT,CP,TH,PH,ALPHA
      NP=NC(IIK)
      DO 53 K=1,NH
      WRITE(6,7) H(K)
7     FORMAT('0',-1PF14.4)
      DO 53 NN=1,NP
      DO 14 I=1,78
14    A(I)=0.0D0
C
C     NON ZERO MATRIX ELEMENTS ON AND BELOW THE DIAGONAL
C     THE SPIN HAMILTONIAN MATRIX ELEMENTS ARE IN GIGAHERTZ
      PC =G  *X*H(K)*DCOS(TH(NN)*DP)
      PS =GP *X*H(K)*DSIN(TH(NN)*DP)
      PIC=GIZ*Y*H(K)*DCOS(TH(NN)*DR)/2.0D0
      PIS=GIP*Y*H(K)*DSIN(TH(NN)*DR)/2.0D0
      AF=(AC-F)/3.0D0
      DF=D/3.D0
      S2=DSQRT(2.D0)
      S5=DSQRT(5.D0)
      EPA =CDEXP((0.0D0,-3.0D0)*(PH(NN)-ALPHA(NN))*DR)
C     DIAGONAL
      A( 1)= 2.5*PC - PIC -    AF + 10.*DF + 1.25*AI - 125./24.*U(1)
      A( 3)= 2.5*PC + PIC -    AF + 10.*DF - 1.25*AI + 125./24.*U(1)
      A( 6)= 1.5*PC - PIC + 3.*AF -  2.*DF + 0.75*AI -   9./8. *U(1)
```

```
      A(10)= 1.5*PC + PIC + 3.*AF -  2.*DF - 0.75*AI +    9./8. *U(1)
      A(15)= 0.5*PC - PIC - 2.*AF -  8.*DF + 0.25*AI -    1./24.*U(1)
      A(21)= 0.5*PC + PIC - 2.*AF -  8.*DF - 0.25*AI +    1./24.*U(1)
      A(28)=-0.5*PC - PIC - 2.*AF -  8.*DF - 0.25*AI +    1./24.*U(1)
      A(36)=-0.5*PC + PIC - 2.*AF -  8.*DF + 0.25*AI -    1./24.*U(1)
      A(45)=-1.5*PC - PIC + 3.*AF -  2.*DF - 0.75*AI +    9./8. *U(1)
      A(55)=-1.5*PC + PIC + 3.*AF -  2.*DF + 0.75*AI -    9./8. *U(1)
      A(66)=-2.5*PC - PIC -    AF + 10.*DF - 1.25*AI + 125./24.*U(1)
      A(78)=-2.5*PC + PIC -    AF + 10.*DF + 1.25*AI - 125./24.*U(1)
C     FIRST   SUB-DIAGONAL
      A( 2)=-PIS
      A( 5)=S5*(BI/2. - 13./12.*U(3))
      A( 9)=A(2)
      A(14)=S2*(BI    - 11./3. *U(3))
      A(20)=A(2)
      A(27)=(3.*BI/2. - 25./4. *U(3))
      A(35)=A(2)
      A(44)=A(14)
      A(54)=A(2)
      A(65)=A(5)
      A(77)=A(2)
C     SECOND  SUB-DIAGONAL
      A( 4)=S5*PS/2.
      A( 8)=A(4)
      A(13)=S2*PS
      A(19)=A(13)
      A(26)=1.5*PS
      A(34)=A(26)
      A(43)=A(13)
      A(53)=A(13)
      A(64)=A(4)
      A(76)=A(4)
C     FIFTH   SUB-DIAGONAL
      A(16)= 1.5*U(4)*S5*EPA
      A(31)= 1.5*U(4)*EPA
      A(50)=-A(31)
      A(73)=-A(16)
C     SIXTH   SUB-DIAGONAL
      A(22)=( 2./3.*AC + U(2)/2.)*S5*EPA
      A(30)=( 2./3.*AC - U(2)/2.)*S5*EPA
      A(39)= U(2)*S2*EPA
      A(49)=-A(39)
      A(60)=-A(30)
      A(72)=-A(22)
      CALL EIGCH(A,N,IJOB,S,Z,IZ,WK,IER)
      DO 11 J=1,6
11    DEL(J)=(S(14-2*J) - S(13-2*J))*1.0D3
      KVI=NR*(K-1) + NN
53    WRITE(6,10) CP(NN),DEL,(VI(KVI,J),J=1,6)
10    FORMAT('0',T12,A4,T27,'FIT',T31,6F10.3/' ',T27,'EXP',T31,6F10.3)
      STOP
      END
```

G = 2.003 GI = 0.180

THE PARAMETERS AC,D,F,AI,BI,U ARE IN MHZ

AC = 392. D =-252. F = 11.

AI = -32.250 BI = -32.250

U1 = 0.007 U2 = -0.005 U3 = -0.005 U4 = -0.005

JBB RB GA H ALONG THE 111 AXIS ENDOR FIT

SITE	A	B	C	D
THETA	0.0	70.5	109.5	70.5
PHI	0.0	60.0	0.0	-60.0
ALPHA	9.5	-9.5	9.5	-9.5

H IN T		ENDOR FREQUENCY IN MHZ					
0.3045							
A	FIT	81.243	49.230	17.009	15.131	47.595	80.105
	EXP	0.0	0.0	0.0	0.0	0.0	0.0
B	FIT	81.080	49.175	17.160	15.566	47.573	79.936
	EXP	81.083	49.180	0.0	0.0	47.576	79.931

JSB RB GA H ALONG A CUBIC FIELD AXIS ENDOR FIT

SITE	A	B	C	D
THETA	55.2	63.7	55.2	45.4
PHI	11.0	0.0	-11.0	0.0
ALPHA	9.5	-9.5	9.5	-9.5

H IN T — ENDOR FREQUENCY IN MHZ

0.3337

A	FIT	81.175	49.169	17.503	15.540	47.619	79.993
	EXP	81.171	49.179	0.0	0.0	47.650	79.985
B	FIT	81.159	49.176	17.874	15.991	47.546	79.964
	EXP	0.0	49.179	0.0	0.0	47.546	0.0
C	FIT	81.165	49.387	17.933	15.960	47.805	79.981
	EXP	81.171	49.370	0.0	0.0	47.792	79.985
D	FIT	81.195	49.470	17.295	15.343	47.939	80.025
	EXP	0.0	49.471	0.0	0.0	47.947	0.0

BIBLIOGRAPHY

[1] R.deL. Kronig and C.J. Bouwkamp, Physica 6, 290 (1939).

[2] B. Bleaney and R.S. Trenam, Proc. R. Soc. A223, 1 (1954).

[3] C.P. Poole,Jr., Electron Spin Resonance, Interscience, New York, 1967.

[4] A. Danilov and A. Manoogian, Phys. Rev. B6, 4097 and 4103 (1972).

[5] A. Abragram, The Principles of Nuclear Magnetism, Oxford Press, p. 40, 1961.

[6] H. Lipson, Proc. R. Soc. A151, 347 (1935).

[7] H. Lipson and C.A. Beevers, Proc.R. Soc. A148, 664 (1935).

[8] G.E. Bacon and W.E. Gardner, Proc. R. Soc. A246, 78 (1958).

[9] H.M.L. Pryce, Proc. R. Soc. A63, 25 (1950).

[10] S. Geschwind, Phys. Rev. 121, 363 (1961).

[11] P. R. Locher and S. Geschwind, Phys. Rev. 139, A991 (1965).

[12] G.E. Pake and T.L. Estle, The Physical Principles of Paramagnetic Resonance, 2nd ed., W.A. Benjamin Inc.,p. 97, 1973 .

[13] W. Low, Paramagnetic Resonance in Solids, Solid State Physics, Supplement 2, Academic Press, 1960 .

[14] A. Abragam and B. Bleaney, Electron Paramagnetic Resonance of Transitions Ions, Clarendon Press, Oxford Press, 1970 .

[15] The IMSL Library Volume 1, 5th ed., International Mathematical Statistical Libraries Inc., Houston, Texas, 1975 .

[16] S. Geschwind, Phys. Rev. Lett. 3, 207 (1959)

[17] H. Watanabe, Prog. theor. Phys., Osaka 18, 405 (1957).

[18] A. Larson and D. Cromer, Acta Cryst. 22, 793 (1967) .

[19] J.W. Culvahouse and L.C. Olsen, J. chem. Phys. 43, 1145 (1965).

[20] S. Aisenberg, H, Statz and G.F. Koster, Phys. Rev. 116, 811 (1959).